

Title:

A novel fiber-fretting test for tribological characterization of the fiber/matrix interface

Authors:

Joey Kabel^a, Thomas E. J. Edwards^b, Caroline Hain^{b,c}, Tatiana Kochetkova^b, Darren Parkison^a, Johann Michler^b,
Peter Hosemann^a (Corresponding Author: peterh@berkeley.edu)

Affiliations:

^aUniversity of California Berkeley, Department of Nuclear Engineering, 4151 Etcheverry Hall, Berkeley, CA
94720, USA

^bLaboratory for Mechanics of Materials and Nanostructures, Empa Swiss Federal Laboratories for Materials
Science and Technology, CH-3602 Thun, Switzerland

^cBern University of Applied Sciences, Institute ALPS, Laboratory for Plasma Surface Engineering, Quellgasse
21, 2502 Biel/Bienne, Switzerland

Abstract

Ceramic matrix composites exhibit excellent high temperature properties and are candidate materials for structural applications from jet engines to nuclear fuel cladding. The strength and deformation behavior of these composites are intrinsically tied to the properties of the fiber/matrix interface. This research introduces a novel technique to evaluate the fundamental friction and wear characteristics of these interfaces. A case study on SiC_f/PyC/SiC_m composites applies *in situ* fiber fretting to investigate the kinetic friction coefficient and cyclic wear characteristics of the interphase. The experimental methodology is presented in explicit detail to encourage other researchers to explore the capabilities of this technique. Testing was carried out as a function of fiber roughness, PyC thickness ($\approx 10, 500, 1200$ nm), cycle count (10, 100, 1000), and frequency (1, 5, and 10 Hz). The friction coefficient and wear behavior changed with cycle length due to a transition from adhesive to abrasive mechanisms. SEM fractography provided insights to

This document is the accepted manuscript version of the following article:
Kabel, J., Edwards, T. E. J., Hain, C., Kochetkova, T., Parkison, D., Michler, J., & Hosemann, P. (2021). A novel fiber-fretting test for tribological characterization of the fiber/matrix interface. *Composites Part B: Engineering*, 206, 108535 (16 pp.).
<https://doi.org/10.1016/j.compositesb.2020.108535>

This manuscript version is made available under the CC-BY-NC-ND 4.0
license <http://creativecommons.org/licenses/by-nc-nd/4.0/>

tribological evolution from adhesive sliding to three-body abrasive wear. The structural disorder at the tribo-surface relating to graphitic content and dangling bond density was investigated using Raman spectroscopy. Properties are contextualized with comparison to uniaxial tensile behavior of the parent composite.

Keywords: Ceramic-matrix composites (CMCs), Interface/interphase, Friction, Wear, Micro-mechanics, fiber push-out

1 Introduction

Ceramic composites exhibit toughness via microcrack formation and subsequent deflection at the fiber/matrix interface. Under vibrational loading, these micro-cracks open and close causing cyclic wear of the debonded interface [1]–[3]. The frictional resistance and degradation of this interface govern the local load distribution, where over-loading and frictional pinching of the fiber can initiate composite failure [4]–[7]. This is especially true in oxidizing environments [8], [9]. Fiber push-out and composite hysteresis testing have been industry standards for evaluating the fiber/matrix interface properties responsible for global behavior [10]–[15]. Fiber push-out tests, as well as micro-pillar compression, provide direct property extraction but are limited in their ability to characterize degradation over time. Hysteresis testing of mini-composites provides information on the macroscopic behavior but requires complex deconvolution of the stress-strain data to estimate the interfacial degradation [5], [16]–[19]. These estimates are then re-integrated into non-dimensional parameters and applied to the predictive models [4], [6]. The fidelity of these models could be vastly improved with direct extraction of the tribological properties and responsible mechanisms. Given these characteristics, other parameters and assumptions in the model can be challenged with confidence in the underlying constituent behavior.

In recent years, accelerated evolution of small-scale mechanical testing has provided a variety of systems and expertise that enable unique and approachable experiments [20]–[22]. With scientific motivation and state of the art equipment, a new technique was developed that could supplement previous methods to provide more applicable friction data for constitutive models. The method, termed “fiber-

fretting”, applies a typical scratch stage and modified indenter tip with integrated transducer to grab, debond, and cycle an isolated fiber segment. Control over the applied compressive load alleviates some uncertainties regarding residual stress and shear lag normally associated with fully constrained tests [18], [23], [24]. Furthermore, the process relies on a relatively simple combination of mechanical polishing and focused ion beam (FIB) milling techniques. This research is intended to be a simple method for probing constituent level tribo-properties of the as-fabricated composite, across a variety of environments.

Here, this methodology is explored with a case study on silicon carbide composites ($\text{SiC}_f/\text{SiC}_m$) with pyrolytic carbon (PyC) bond layer at the fiber/matrix interface. These composites express excellent high temperature strength, toughness, chemical stability, and irradiation tolerance making them preferred candidates for application in advanced nuclear and aerospace applications.

1.1 Tribological considerations

Tribological characterization aims to understand the interplay between the observed experimental properties and the responsible mechanisms. According to the law proposed by Bowden and Tabor [25], the friction force P_X evolves by combination of adhesion force F_A and ploughing force F_P , that is,

$$P_X = F_A + F_P \quad (1)$$

where F_A depends on active bonding sites and shear strength of the contacting surfaces, and F_P on surface roughness and hardness. Additional factors including wear debris, velocity, lubrication, and environment drive the associated wear mechanisms and resulting friction coefficient [25], [26].

Adhesive wear is governed by local welding at the contacting surfaces and subsequent debond and transfer of that material [25]–[27]. Resistance increases when surface bonding is favorable, e.g., between similar materials, when dangling bonds are present, and in vacuum. Resistance decreases when the active bonding sites are passivated, for example when surfaces oxidize. Abrasive friction is common for hard ceramic materials and typically governed by asperity fracture and plowing that causes third body wear

debris [27]. These particles exacerbate plowing and thereby increasing relative contribution of F_p . Both friction coefficient and wear rates typically increase in abrasive conditions compared to adhesive.

In this study, the friction system consists of interfacing SiC surfaces with the PyC solid lubricant bond layer. The fracture location and PyC thickness (h_{PyC}) relative to the max fiber surface roughness (R_{max}) determines the degree of SiC on SiC asperity interaction. For $h_{PyC}/R_{max} < 1$, the sliding resistance is likely governed by SiC asperity shearing and plowing. For $h_{PyC}/R_{max} \approx 1$ mixed shearing contribution from SiC and PyC is expected. For $h_{PyC}/R_{max} \gg 1$, failure can be adhesive at the SiC/PyC interface or cohesive within the PyC. The former suggests mixed shearing from PyC and SiC, while the latter is exclusively shearing of the PyC.

Tribological behavior of SiC and graphite are well studied across many material allotropes, couples, and environments [28]–[34]. As a brittle ceramic, SiC usually degrades following abrasive mechanisms like asperity chipping and surface cracking. The wear rate is dependent on grain size, texture, and additives, with typical kinetic friction coefficient (μ_k) values between 0.2-0.8 depending on environment. Graphitic materials, like PyC, provide desired lubricity due to weakly bound basal planes of the anisotropic sp^2 ring structure. However, the relatively soft material is subject to structural damage from both mechanical and thermal loading. Degradation of the sp^2 ring structure can introduce active carbon sites that compromise the lubricious quality [35]. Orientation of the basal planes also plays an important role relating to active site density at the tribo-surface [36]. Graphite-like materials are particularly sensitive to environment where both physio-and chemisorption of gasses and moisture can reduce the Van der Waals bonding between the basal planes [31], [35] Increasing temperature, from the working environment or flash heat generated by asperity contact, can promote gas and moisture absorption that helps maintain low friction by passivating these active sites [32]. However, as temperatures approach 500°C, oxide and hydrocarbon volatilization become a major concern. With all of this considered, friction values for graphitic carbon have shown to range from 0.05 to 0.5 depending on environment[31].

Raman spectroscopy is commonly applied to understand the relationship between carbon structure and friction values [34], [37]–[40]. Raman is an excellent tool for carbon characterization with robust analyses developed to quantify myriad characteristics including crystallinity, sp^2 fraction, structure clustering, and bond degradation. There are two prominent peaks in the Raman spectra of graphitic carbon, the D band appearing at $\approx 1355\text{ cm}^{-1}$, the G band at $\approx 1581\text{ cm}^{-1}$. The D band appears due to the A_{1g} breathing mode and requires a defect for its activation. The G band originates from the E_{2g} stretching mode and occurs at all the available sp^2 sites, ring or chain [39]. For nano-crystalline graphite-like CVI PyC, the intensity of the D band relative to the G band (I_D/I_G) reveals information regarding the graphite cluster size and thereby degradation of the clusters. The G peak position provides insight to the amount of structural degradation as sp^2 phonon modes soften with reduced ring structures. Ferrari et al. proposed a phenomenological trajectory that maps the expected G-peak shift and I_D/I_G from graphite to diamond in three stages [39]. Moreover, the G peak width can indicate possible surface structural disorder, such as variations in bond lengths and angles in sp^2 clusters [41]. Given the spectra evolution for different stages of the test, conclusions can be drawn regarding the damage state of the PyC.

This experiment was developed in SEM vacuum at ambient temperatures for controlled investigation of the material specific properties and mechanisms. However, testing in ambient pressure or in artificially hydrated atmospheres is similarly possible.

2 Experimental

2.1 Experiment design

A single fiber, tow, or woven composite can be polished along the fiber's longitudinal axis to expose the underlying fiber. It should remain embedded in the matrix and have at least one-half of its diameter polished away to minimize residual stresses and avoid complex stress states during testing. FIB milling is subsequently used to polish additional material off the top and to trench two locations that results in an

isolated fiber segment with a semi-cylinder cross section. Figure 1 shows a schematic of the basic segment geometry and testing.

Figure 1 – *INSERT (width = 190mm, color online)*

As the segment slides in Figure 1B, the contact length, $L(x)$, is reduced resulting in a systematic stress oscillation. The center of the segment is always in contact while the segment ends are completely unloaded and reloaded. The mean stress for each region is then dependent on the applied load and amount of lateral displacement. This overhang is user defined. Considerations include matching reality based on observed crack opening in mini-composite tests (see Appendix A), available space for translation as it relates to cost of FIB fabrication, and the machine's load and displacement resolution.

The applied normal load, P , resolves along the arc length of the segment following a cosine relationship, peaking at the centerline ($\vartheta=0$) where the resultant force, P_z , is equal to the prescribed load. This is simplified assuming the peak load acts uniformly on the projected area of the segment, similar to nano-indentation analysis, Figure 1A. Provided the force data, P_x and P_z , the kinetic friction coefficient can be calculated as follows with the Coulomb friction law that assumes contact area independence [27]:

$$\mu_k = \frac{P_x}{P_z} \quad (2)$$

If there is misalignment relative to the scratch direction, the fiber segment may impede on one wall of the channel while separating from the opposite. This produces an additional force in the y axis, P_y , with magnitude that depends on the degree of misalignment. Like P_z , P_y is orthogonal to P_x and therefore contributes to the friction relationship. Assuming the mechanism of frictional resistance is the same for P_y and P_z , they can be summed with vector length $P_{YZ} = \sqrt{P_y^2 + P_z^2}$. The direction of this vector is no longer orthogonal to the projected area, but physically represents a translation of the peak orthogonal load along

the semi-cylindrical fracture surface, depicted in Figure 1C, around which the orthogonal load decays following the aforementioned cosine relationship. Physically this may impact the location of maximum wear in the channel, but otherwise the simple Coulomb relationship holds true and becomes:

$$\mu_k = \frac{P_X}{P_{YZ}} \quad (3)$$

2.2 Materials and fabrication

Single fiber and single tow (≈ 500 fibers) composites, referred to as micro- and mini-composites respectively, were evaluated in this research. General Atomics (GA) manufactured two composite sets that included a micro- and mini-composite. One set was prescribed Hi-Nicalon Type-S (HNLS) fibers and the other an early generation Tyranno S (S) fiber [42]. Chemical vapor infiltration (CVI) was used to consolidate the fiber preforms by depositing a monolayer of pyrolytic carbon (PyC) followed by a dense ($\approx 95\%$) β -SiC matrix. Scanning and transmission electron microscopy (SEM and TEM) was carried out to evaluate the PyC thickness (h_{PyC}), fiber and PyC structure, and provide insight to relative fiber surface roughness. The major difference between each sample is the combination of fiber and PyC thickness, named H-thick, H-thin, S-thick, and S-thin respectively. PyC thicknesses range from 11 nm to 1200 nm, spanning the anticipated design space for an optimized composite [3]. Table 1 outlines the composite characteristics.

Table 1 – Sample characteristics

Name	H-thick	H-thin	S-thick	S-thin
Composite type	Single fiber	Single tow	Single fiber	Single tow
Fiber	HNLS	HNLS	S	S
Fiber tilt (°)	0.3	1.5	0.6	0.8
h_{PyC} (nm)	500	23	1200	11
h_{PyC}/R_{max}	≈ 25	≈ 1	≈ 50	≈ 0.5
R_{RMS} (nm)	4		5	
R_{max} (nm)	20		24	
λ_0 (nm)	26		51	

TEM showed that H fibers exhibited the typical grain structure and roughness characteristics as found in literature [18], [43]. S fibers were highly nano-crystalline with root mean square (R_{RMS}) and max

roughness (R_{\max}) similar to HNLS. The major difference was the asperity wavelength, λ_0 , quantified as the average spacing of zero-point crossings at the mean centerline of the fiber surface, as seen on Figure 2A&B. The S fiber wavelength was found to be twice as large as the H fibers. Deposition parameters for the PyC are proprietary. However, it is known that the precursor gas was a methane/ H_2 mixture, and the conditions were tailored to produce highly oriented nanocrystalline PyC. High resolution TEM near the center of the PyC bond layer of H-thick and S-thick verified this PyC structure, shown in Figure 2C. The (002) lattice fringes were aligned parallel to the fiber surface, which is typical of ordered nanocrystalline CVI PyC [44]. The texture of the PyC was quantified via opening angle (O.A.) analysis [45]. Texture classification proposed by Reznik and Hüttinger [28] follows high texture (HT, $O.A. < 50^\circ$), medium texture (MT, $50^\circ < O.A. < 80^\circ$) and low texture (LT, $180^\circ > O.A. > 80^\circ$). The images were processed with an auto-threshold followed by an FFT transformation using FIJI image processing software [46]. Each FFT was analyzed in OriginPro using the Azimuthal Average Tool to extract grayscale intensity of the (002) diffraction arc as a function of angle. The peaks were fit with a Gaussian and the O.A. was taken as the average FWHM of the two peaks shown in Figure 2D. An O.A. value of 49 suggests the PyC is highly textured.

Figure 2 – *INSERT (width = 90mm, color online)*

Micro- and mini-composites were cut and polished with a Leica EM TXP micro-polishing instrument. Samples were mounted on an aluminum SEM stub with thermoplastic mounting adhesive and polished down to 3 μm diamond lapping film with water lubricant. Figure 3A shows a typical cross-section of the micro-composite with embedded fiber. The integrated stereo microscope allowed incremental observation of the fiber exposure during polishing. Fibers, especially in the mini-composite samples, were not always parallel with the polishing plane. To find a suitably horizontal fiber, material was continuously removed until an exposed fiber exhibited an ellipsoidal cross-sectional with aspect ratio at least $\approx 1:40$, corresponding to

an embedded tilt of $< 1.5^\circ$ [14]. This tilt has implication regarding segment plowing during the fretting tests. Polishing was terminated when the exposed fiber diameter was maximized, having reached the center plane of the longitudinal axis. The micro-composites were only 300 μm in diameter and therefore delicate. As a result, the mechanical polishing sometimes induced matrix cracking and debonding of the PyC, as was the case for composite S-thick. This impacted the ability to extract an initial debond strength but did not limit the evaluation of subsequent kinetic friction.

The segment structures in Figure 3B, termed “micro-sliders”, were fabricated via Ga^+ FIB with a dual beam Tescan Vela microscope. Beam conditions were set at 30keV with rough cuts made at 12nA followed by 1nA polishing. Fiber segments of $\approx 15 \mu\text{m}$ length were fabricated via stair-step FIB trenches $20 \times 10 \times 8 \mu\text{m}^3$ ($W \times L \times H$). The trench size was optimized to accommodate the gripper and reduce milling time, allowing up to 5 μm of lateral translation. Ga^+ penetration depth at these conditions is expected to be less than 50 nm [47], [48], affecting less than 0.1% of the active friction surface. These FIB cuts are very simple and translate well for large sample yield. The semi-cylinder cross-sections of the H and S composite samples are shown in Figure 3C. Dashed lines overlay the PyC interface of H-thin and S-thin to emphasize the location as the PyC is difficult to see. The images also show representative defects commonly observed at the interfaces including porosity and carbon nodules spurring from surface contaminants or CVI turbulence during deposition [45]. In total, six micro-sliders were fabricated for composites H-thick and S-thick, and four each for H-thin and S-thin.

Figure 3 – *INSERT (width = 140mm, color online)*

2.3 Testing

The goal of the fiber fretting test is to gain fundamental understanding of constituent properties as it relates to composite behavior. To explore this relationship, mini-composite samples H-thin and S-thin were

also tested in uniaxial tension inside the SEM. Testing was designed to observe damage evolution in the form of matrix crack spacing, L_s , and crack opening, L_o . This spacing is characteristically periodic and related to an approximated interfacial sliding stress [3], [49], τ_s , that can be contrasted to the direct fiber fretting values. The average micro-crack opening was $\approx 2 \mu\text{m}$, representing realistic interfacial translation that was then used to define cyclic displacement for the fretting tests. The tensile experiment and analysis are described in Appendix A.

The fretting experiment was developed using an Alemnis standard assembly indenter with scratch stage and SmarTip add-ons. Compressive load was applied with a Z-displacement piezo-stack driver in closed-loop displacement control. A 0.5N load cell behind the sample recorded the initial load prior to fretting, as the load cell later becomes unreliable due to torqueing with lateral load. Cyclic fretting was applied with a piezo-driven scratch stage in open-loop displacement control. The scratch stage holds both the load cell and the sample, meaning the substrate moves while the fiber segment is held stationary by the gripper. The gripper is screwed to a SmarTip transducer that is mounted to the Z-displacement piezo-stack. The SmarTip is optimized for instantaneous output of the P_x , P_y , and P_z forces as the substrate is displaced. This transducer consists of four independent piezo sensors that measure instantaneous potential during the test. P_x and P_y forces are calculated from differential potentials of the orthogonal axisymmetric pairs (i.e. piezo 1 and 3 for P_x in Figure 4A), while P_z is calculated as the sum of all four electrodes. Figure 4C shows the physical system and associated components. Alemnis AMICS software was used to control the closed-loop Z-displacement of the tip. An additional software, Meaure3.0, communicated with the National Instruments DAQ to simultaneously control the scratch stage and acquire the displacement and SmarTip data.

Two gripper designs were explored for latching the indenter tip to the fiber segment. The first uses a conical diamond tip. In this case, a hole is FIB milled at the center of the segment without penetrating the underlying interface. The tip is inserted into the hole with a predefined load and then held at that Z-position during lateral motion. This configuration can promote self-alignment of the segment within the channel during lateral motion, like a ball and socket load train for tensile testing. However, this has other

implications such as segment tilting and plowing effects that may stray from reality of a constrained composite. The second approach uses a “claw” gripper that contacts both ends of the segment to hold it flat during translation, thereby minimizing plowing effects. This rigidity can result in alignment sensitivity when the contact points or segment orientation are misaligned relative to the scratch direction. Since alignment issues can be overcome with experimental diligence, the claw gripper was expected to be more robust and was subsequently used after initial proof of concept testing with the conical tip. Figure 4A,B show SEM images of the two grippers.

The claw gripper was FIB milled from a conical tip. The geometry was designed to minimize stress concentration and withstand the expected shear stress. Testing with the conical tip revealed that the 3 μm diameter mark of the cone could withstand the induced shear stresses. As a result, the ends of the claw arms were prescribed 3 μm equivalent diameters. The interior of the claw was prescribed a 10 μm radius of curvature. Special effort was given to produce a peak along the centerline of the claw interior by over- and under-tilting the stage during FIB milling. This was done to promote a single point of contact at the segment edges to improve contact alignment relative to the scratch axis.

Figure 4 – *INSERT (width = 140mm, color online)*

The entire test apparatus was tilted at 22 degrees in the SEM. This allowed for reasonable visibility of the gripper curvature and fiber segment allowing for optimized alignment. Tip alignment was done simply by evaluating the symmetry of the claw in the SEM and iteratively rotating until symmetric. The relative orientation of the axisymmetric sensors was unimportant as the values can be mathematically rotated in the software after the fact. Thereby it is more important to have the fiber exactly aligned with the scratch direction to avoid influence from the channel side walls. This alignment was done by measuring the observed angle of the interface relative to horizontal with careful attention to the SEM stage and image

rotation. If either the fiber or claw were misaligned, the system was vented, stub and/or tip manually rotated, and then re-pumped to checked again. This alignment procedure could be easily improved with an automated piezo rotation stage. All samples were successfully aligned to $\pm 1.5^\circ$. This was sat factory as the loads induced in the Y direction were minimal and can be corrected for by adding it the Z-force as described in equation 3 in the experiment design section.

To perform the test, the fiber segment was postioned below the gripper using the piezo stage control. The tip was brought into contact with the sample (<0.1 mN) and the stage was adjusted in X and Y with 10 nm steps until the residual load was minimized. This was done iteratively until the segment was centered with the gripper. The test was initiated in displacement control at 100 nm/s to reach a set-point load (P_o) and then held at that Z-displacement. To keep the true contact area (relating to asperity and surface roughness interaction) consistent from test to test, P_o was adjusted per sample to achieve an average pressure (σ_o) ≈ 70 MPa. This was calculated with the projected area of the longitudinal cross-section, ranging from 144 to 222 μm^2 depending on amount of the fiber polished away and segment length. The starting values and test conditions are further outlined in *Table 2*. Fretting was then applied with a triangle wave form to complete a specific number of cycles (N) at a given frequency. One cycle is defined as a complete translation of the substrate; 2 μm right, 4 μm left, and 2 μm right, returning to the start position. This equates to 8 μm total sliding distance per cycle, corresponding to 8, 40, and 80 $\mu\text{m/s}$ sliding velocity for 1, 5, and 10 Hz respectively. Data was sampled at 200 Hz.

2.4 Characterization

To investigate the tribo-surface after the test, the fiber segment needed to be removed. This was achieved by pushing the segment laterally with a tungsten tip manipulator typically used for TEM sample lift-outs. The segment was weakly bound and would often eject upon initial contact. The underlying surface was then available for SEM inspection and Raman spectroscopy. The morphology of the worn surfaces was characterized with a field emission FEI Quanta SEM. Raman spectroscopy was performed using a Renishaw inVia machine with excitation wavelength of 488 nm at 1 mW with signal collection time of 10 seconds and

single accumulation. The spectra were taken from 0-2000 cm^{-1} to capture SiC bands between $\approx 700\text{-}1000\text{ cm}^{-1}$ and the two prominent graphitic carbon bands from $\approx 1300\text{-}1700\text{ cm}^{-1}$. Scans were taken at the center where the rubbing surfaces were in continuous contact, shown in the SEM image of Figure 5. It is expected that during composite operation, most interfacial friction occurs under continuous contact conditions. Therefore, the carbon structure at the center is more representative of a realistic degradation state. Spectra processing was performed using a custom Python code and included background removal, with D and G peak fitting using two Lorentzian functions, shown Figure 5. The peak positions, intensities, and full width at half maximum (FWHM) were extracted to quantify the spectra evolution. The example shown in Figure 5 is from an uncycled fracture surface of sample S-thick. This spectrum is tabulated in the discussion and is considered a reference value for CVI PyC.

Figure 5 – *INSERT (width = 90mm, color online)*

3 Results

3.1 Fretting test

Early testing with the conical tip on composite S-thick found that the conical tip splits the fiber segment as loading approached $\approx 40\text{ mN}$. This limited the achievable stress and motivated exploration of cycle and frequency dependence at a fixed pressure. A successful conical tip test is shown in the vertical sequence on the left of Figure 6. This tip-segment coupling allowed for tilting during translation, highlighted by the red lines. The test video (see supplementary video, V_S-thick-1) showed very thin layers of PyC being shaved and pushed aside with each translation, suggesting the leading edge of the segment is acting as a plow. In a real composite, this type of behavior might be observed at a broken fiber away from the microcrack or at the composite surface if fibers are left exposed. However, for components under vibrational loading near the proportional limit stress, matrix cracking and interfacial debond typically

precede fiber failure. Therefore, it is expected that frictional contribution in real applications occurs along the continuous interfacial regions. The claw gripper was applied to limit the influence of lead edge plowing, shown on the right-hand side of Figure 6. The difference in PyC extrusion is pronounced comparing the final image of the 1000 cycle claw test to the 50 cycle conical tip test.

Figure 6 – **INSERT (width = 140mm, color online)**

Fourteen samples across four interface conditions were successfully tested with the claw gripper. *Table 2* outlines the composite sub-samples and experimental conditions applied to each. Variability in σ_0 was attributed to the sensitivity of the integral gain controller to pause displacement at the exact P_0 . Although pressure dependence is consistently observed in tribological studies, the values here range ± 20 MPa compared to most studies that vary at least ± 200 MPa that ultimately observe small variation of μ_k [32]. These variations are not expected to have a significant impact. A slower displacement loading rate would improve accuracy. Supplementary data provides a representative test video of each composite type, as well as a conical and claw test on the S-thick sample.

Table 2 - Fiber fretting test matrix

Composite	Sample	Cycles	Frequency (Hz)	Proj. area (μm ²)	P _o (mN)	σ _o (MPa)
H-thick	1 ⁺	100	1	208	17.2	83
	2 ⁺	100	5	211	18.1	86
	3 ⁺	100	10	222	6.5**	29
	4	10	1	213	15.7	74
	5	100 + 900	1	214	17.8	83
	6	1000	1	212	15.3	72
H-thin	1	10	1	144	8.08	56
	2	100	1	144	8.79	61
	3	1000	1	150	9.83	66
S-thick	1**	50	0.25	173	21.6	125
	2	10	1	164	10.5	64
	3	100	1	165	10.5	64
	4	1000	1	172	11.8	69
S-thin	1	5	1	180	14.6	81
	2	20	1	183	14.1	77

⁺ Segment with center hole

^{*}Conical tip test with 3 μm translations

^{**}Load dropped at start of test as segment readjusted to center of gripper

Force data from the load cell and SmarTip were combined for friction evaluation. The load cell captured the P_o prior to lateral motion. The tip sensors, optimized for short-time measurements, captured the instantaneous load (P_z) from cycle to cycle but were susceptible to global drift over the course of the test. Drift was removed via background subtraction using asymmetric least squares fitting with symmetry factor = 0.5 and smoothing factor of 10 (OriginPro 2020) to follow the centerline of the oscillatory load. The corrected P_x data was kept centered around zero while the other orthogonal contributing forces (P_o, P_z, and P_y) were summed to find P_{max} as described in the experiment design section. As a result, the instantaneous value for the kinetic friction coefficient throughout the test is given by:

$$\mu_k = \frac{P_x}{\sqrt{(P_o + P_z)^2 + P_y^2}} = \frac{P_x}{P_{max}} \quad (4)$$

An example of the data analysis process is shown in Figure 7, expressing the first 100 cycles of sample H-thick-4. Baseline fits for global drift subtraction are overlaid in green in Figure 7A. P_{max} is shown as

the blue curve, P_x as red, and μ_k as purple in Figure 7B. As the displacement is oscillatory, there is a turnaround point where P_x crosses zero. The useful data is at steady-state sliding between these turnarounds, observed in the zoom window of Figure 7C. An important characteristic to understand is influence of sliding direction. An ideal test, assuming a constant friction coefficient, would present a plateau in the steady-state region. Mirrored behavior in this regime suggests minimal influence from lead-edge plowing that may occur with a tilted fiber. Composite H-thick is the flattest with tilt angle ≈ 0.3 degrees. Indeed, nearly identical behavior is observed sliding left versus right shown in Figure 7B,C. This is consistent for all H-thick micro-sliders. Samples with large fiber tilt like H-thin at 1.5° sometimes showed transient behavior with either a sloped plateau or non-mirrored shape, suggesting different effects due to sliding direction. To be conservative while also capturing friction behavior over time, envelope curves are fit to the peak friction of each cycle. The upper and lower envelopes correspond to the substrate sliding right and left, respectively, shown as the solid black and dashed line overlaid on the μ_k curve of Figure 7C. For comparison between composite types, the friction envelope corresponding to the segment sliding “down” the embedded incline was taken where lead-edge plowing is assumed to be minimized. Globally, the shape of the envelope gives insight to the governing mechanisms of friction. The envelope curves for each sample are presented in succession, categorized by their parent composite and test conditions. Adhesive and abrasive mechanisms are assigned based on friction values and tribo-surface characterization.

Figure 7 – *INSERT (width = 190mm, color online)*

3.2 Composite H-thick

Six micro-sliders were tested with the claw gripper on composite H-thick, shown earlier in Figure 3B. These samples failed at the PyC/fiber interface which is typical for these composites [13], [14], [50]. As a result, the interacting surfaces were a combination of PyC and SiC with fracture roughness expected to

follow that of the fiber surface. Considering $h/R_{\max} = 25$, no SiC on SiC interaction was expected or observed.

Figure 8 shows the friction coefficient versus cycle for all six H-thick micro-sliders. Substrate sliding right corresponds to translation down the incline and is used for comparison. Globally, there are three distinct regimes: 1) a smooth decreasing steady-state regime with relatively low friction values in the first ≈ 100 cycles, followed by 2) an aggressive transition with peak resistance, leading to 3) a rough steady-state regime again with decreasing values.

The first regime shows a relatively smooth and decreasing friction coefficient. Samples H-thick-1, 2, and 3 were carried out to 100 cycles at 1, 5 and 10 Hz, respectively. The 1 Hz and 10 Hz samples show similar values while the 5 Hz sample shows reduced friction. This does not suggest a meaningful trend but rather that scatter exists. This is supported when incorporating H-thick-4, 5, and 6 that were tested at 1 Hz, and express friction values spanning the same range as the frequency tests. Sample H-thick-6 even fluctuates within these bounds before transitioning to the high friction regime. The four samples that stopped after 100 cycles show smooth tribo-surfaces in Figure 9 with small flakes or seemingly smeared features. It is proposed that adhesive wear mechanisms govern the low and relatively smooth friction values in this regime. Ultimately it is thought that neither the frequency nor FIB center hole had significant influence on the friction data. Scatter is attributed to small flaking defects and adhesive transfer events. As a result, average curves were established and plotted for both the low friction and high friction regimes, as depicted in Figure 8.

Figure 8 – *INSERT (width = 90mm, color online)*

Looking at the tribo-surface of the 1000 cycle samples in Figure 9, H-thick-5 and H-thick-6 show significant deterioration of the PyC with scattered wear debris. In situ test videos (see supplementary video, V_H-thick-6) linked physical events to the transition events observed in the data. For example, H-thick-6

showed progressive wear product evolution leading to a momentary seize of the segment at cycle 87 followed by ejection of two PyC fragments near the corner edges. The debonded fragments are verified by SEM in Figure 9F. The onset of wear products prior to catastrophic failure suggests fatigue. As the segment cycles, the 2 μm regions at the edges of the sliding channel are cyclically covered and uncovered. Hertzian contact mechanics suggests the leading-edge will induce compression and tensile forces as the segment approaches and retracts respectively over this region [51]. It's expected that the oscillating stress drives microcracking within the PyC depending on the crystallite orientation and pre-existing defects. This opens a path for third-body particle evolution that leads to further break down of the PyC. It is proposed that this introduces wear debris and transitions the friction system from adhesive to abrasive mechanisms. This increases the friction coefficient and sustains wear debris evolution over the remaining 1000 cycles. It should be noted that particles near the center of the tribo-surface appear to roll up, as visible in Figure 9F. These may have evolved to minimize resistance and act as roller bearings. The gradual decrease in friction coefficient out to 1000 cycles supports this.

Raman spectroscopy scans were taken at the center of each tribo-surface and are presented in Figure 9G. In all cases, the data underwent background subtraction and intensity normalizing. Clear degradation of peak shape is observed for both 1000 cycle samples. The 10 and 100 cycle samples are relatively similar in magnitude and shape. Detailed evaluation for I_D/I_G , G peak position, and FWHM versus cycling for all tested composites is presented in the discussion.

Figure 9 – *INSERT (width = 190mm, color online)*

3.3 Composite H-thin

Three micro-sliders were tested on composite H-thin. Failure location was assumed along the PyC/fiber interface, though the PyC layer with $h/R_{\text{max}} \approx 1$ signifies a mixed regime that may have partially

interacting SiC asperities. This sample had the largest embedded fiber tilt at ≈ 1.5 degrees. Again, substrate sliding right was the direction moving down the embedded fiber tilt incline and is presented for comparison.

Figure 10 – *INSERT (width = 90mm, color online)*

The initial friction values range from 0.6 to 1.1, followed by somewhat erratic behavior with peak values in the first 100 cycles. These initial values are large for any friction system containing carbon and suggests significant interaction of the SiC asperities. It is expected these asperities fractured and dulled in the transition regime. This is supported by the 1000 cycle sample that shows the friction values drop around 100 cycles and reach a turbulent steady-state that increases slightly over the remaining 900 cycles. Tribo-surfaces and Raman spectra are shown in Figure 11. Progressive wear product evolution is observed at the center of the tribo-surfaces, appearing to roll up similarly to, however, more pronounced than H-thick-6 in Figure 9F. There was also significant porosity in the underlying matrix that may have impacted friction in two ways, i.e. directly interacting as sharp edges or acting as an avenue for wear product removal. The turbulent steady-state behavior and third body particles suggests abrasive friction. The Raman spectra is plotted to include both the SiC and carbon peaks. Carbon material is still present on all surfaces but thin enough for the SiC signal to come through. For H-thin-3, the $\approx 1 \mu\text{m}$ laser spot size probed both the rolled asperity and surrounding surface. The increased SiC intensity, combined with the degraded carbon peaks, suggests most of the PyC layer was collected in the rolled particles leaving underlying SiC exposed.

Figure 11 – *INSERT (width = 190mm, color online)*

3.4 Composite S-thick

Four micro-sliders including the conical tip test were successfully evaluated. During sample preparation a concentric crack evolved at the center of the PyC bond layer, visible in Figure 3C. This meant that both interacting surfaces were PyC. The bond layer is thick with $h/R_{\max} \approx 50$, further limiting the likelihood of SiC on SiC interaction. Figure 12 presents the relevant friction data.

Figure 12 – *INSERT (width = 90mm, color online)*

The start of the tests shows large variation with increasing friction through ≈ 20 cycles. This is followed by erratic and globally decreasing behavior through 200 cycles. The remaining 800 cycles for S-thick-4 show a steady-state regime slowly decreasing to $\mu_k \approx 0.25$. The conical tip test, S-thick-1, shows an extremely large peak in the first 20 cycles reaching $\mu_k \approx 4$. This is attributed to segment tilt and plowing effects observed in the test sequence images shown in Figure 6. Interestingly, the friction values fall and become consistent with the claw gripped samples (out to 50 cycles). Tribo-surfaces for all S-thick samples are shown in Figure 13. A clean fracture surface from a failed conical tip test that split the segment is shown in Figure 13A&B. Nodule defects from CVI processing are clearly visible here, the protrusions and reciprocal indents are highlighted. This fracture surface is assumed to represent a pure state of the deposited carbon and is used as reference for the Raman data, shown in Figure 13G. Some CVI defects remain visible on the cycled interfaces of Figure 13D-F. In all cases, significant wear debris is observed suggesting abrasive wear. Looking at Figure 13A,D, sharp and flakey debris are seen closely scattered around the CVI defects. It is proposed that these nodules shatter during segment translation, thereby injecting abrasive particles into the rubbing interface. This likely explains the variation and erratic behavior in the early stage of the tests as the particles evolve and then smooth out or get removed. There is some evidence of PyC rolling observed in the

1000 cycle sample, H-thick-4. Raman spectra again shows increased peak broadening and G-peak shift left for increasing cycle number, as seen in Figure 13G.

Figure 13 – *INSERT (width = 190mm, color online)*

3.5 Composite S-thin

Composite S-thin has the thinnest PyC bond layer with $h/R_{\max} \approx 0.5$, promoting SiC asperity interlocking and limiting lubrication of the PyC. Only two tests successfully dislodged at initiation, two others remained locked in place. Video of S-thin-1 and S-thin-2 revealed only 4 and 10 full cycles before respectively seizing and fragmenting (see supplementary video, V_S-thin-2). Sample S-thin-1 was seized for nearly 150 cycles before finally fragmenting, paying tribute to the durability of the claw gripper as lateral load reached nearly 60 mN (other composite tests were consistently below 10 mN). Friction data for the first 20 cycles of S-thin-1 and S-thin-2 is shown in Figure 14.

Figure 14 – *INSERT (width = 90mm, color online)*

A comparable friction zone is highlighted in blue, defined as the region where both segments are fully translating without any fragmentation. The initial μ_k values range from $\approx 1.1 - 1.5$. However, it is unlikely that these values represent a steady-state behavior based on the early cycle behavior of the other composite tests. The friction resistance of the seized segment hovers around 1.6, nearly double of any other steady-state value observed, which is very large and suggests an asperity feature locking mechanism. This type of fragmentation, shown in Figure 15A,D, is not typically observed in real composite failure. The stress concentration and sliding at gripper contact is likely responsible, providing insight to the limitations of this

test. Figure 15C shows a S-thin segment that could not be dislodged, revealing contact marks at the gripper/fiber couple that validate gripper design and successful alignment. The Raman data in Figure 15G shows both carbon and SiC peaks, suggesting PyC still coats the underlying matrix. Although S-thin-2 only saw 10 cycles before fragmentation, there is evidence of PyC rolling up as third-body particles similarly to H-thick and H-thin composites. This suggests the rolling phenomenon initiates early for samples with very thin PyC, likely due to rapid degradation of the carbon from sharp SiC asperities. Ultimately, these tests are considered incomplete as only the first ≈ 5 cycles could be effectively compared.

Figure 15 – *INSERT (width = 190mm, color online)*

4 Discussion

4.1 Comprehensive evaluation

The experimental results demonstrate the capability of the fiber fretting technique to extract friction data and related mechanisms. The most pronounced trend is friction dependence on wear debris as it relates to adhesive and abrasive wear mechanisms. This is showcased clearly by composite H-thick that expresses both low and high friction regimes correlated with smooth and rough tribo-surfaces. Figure 16A,B compares the adhesive and abrasive steady-state regimes for all composites except S-thin that fragmented too early. The line plots for H-thick are averages while H-thin and S-thick each had one sample reach steady-state behavior. Each regime was normalized to a 0-cycle start point and fit with a linear approximation and 95% prediction bands. Here the intercept represents an initial friction value assuming steady-state is achieved, and the slope a coefficient degradation parameter. These fits are tabulated for reference in Table 3 with other relevant characteristics of the friction surface that may be applicable to composite modelling and design. The behavior within each regime is evaluated by considering the relative contributions of F_A and F_P expressed in equation 1.

INSERT Figure 16 – (*width = 90mm, color online*)

Raman analysis provides insight to F_A as it relates to graphite degradation and dangling bond density. Spectra are deconvoluted using a double Lorentzian function to identify the peak intensities, position, and FWHM as a function of cycle. In all cases, peak broadening is observed with increasing cycles, the G-peak FWHM versus cycling is plotted to quantify this effect in Figure 17. It is proposed that continuous cycling induces structural disorder by breaking apart the graphite ring structure in a random manner. This process results in multiple carbon molecule configurations, causing an overall broadening of the Raman spectra from overlapping of the associated peaks [52], [53]. Additionally, the I_D/I_G and G-peak position for all micro-sliders are plotted and compared to the phenomenological trajectory proposed by Ferrari [54] in Figure 17. It should be noted that the aim of this comparison is to follow the change in G-peak position and I_D/I_G values to determine the structural evolution with cycling, without attempting to quantify sp^2 vs. sp^3 content. Increased cycles showed decreasing I_D/I_G and G-peak position, representing the reduction in six-fold ring clustering and increased dangling sp^2 bonds, respectively. With the general trend showing I_D/I_G and G-peak position decrease, it suggests PyC is in stage two of the trajectory. This is expected as CVI PyC characteristically expresses a nano-crystalline graphite structure.

Figure 17 – **INSERT** (*width = 140mm, color online*)

4.2 Adhesive friction

Looking at the adhesive regime of composite H-thick in Figure 16A, the friction data shows a steep decline in coefficient. When compared with corresponding Raman data, Figure 17A, almost no change in

I_D/I_G and G-peak position is observed across these 100 cycles. This suggests the graphite planes are sliding easily and there are no abrupt events altering the graphite ring clusters or structure. This is supported by the smooth tribo-surfaces observed in Figure 9. Two mechanisms are proposed to explain the decreasing coefficient. The first is that gaseous absorption between graphite planes or passivation of the active bonding sites are reducing contribution of F_A . Although possible this was unlikely under SEM vacuum conditions. Of course, SEM vacuum is not perfect and frictional heating could have accelerated passivation with limited gas density. Temperature rise at the friction surface was estimated with the following equation²⁵ that relates heat input and heat removal:

$$\Delta T = \frac{\mu P v}{4a(k_{SiC} + k_{PyC})} \quad (5)$$

where μ is the friction coefficient, P is the applied load, v is the sliding velocity, a is the contact radius set to half segment length (7.5 μm), and k is the thermal conductivity conservatively set to 25 W/mK for SiC and PyC [26]. A hypothetical extreme case was calculated for 10 Hz (80 $\mu\text{m/s}$), 20 mN load, and $\mu = 0.8$. The peak temperature rise is in the order of 10^{-4}K . This is extremely low, attributed to the insignificant load and velocity. This also supports the observed lack of friction dependence on frequency, without temperature rise most velocity effects are diminished [27]. Ultimately it is thought F_A is constant and not responsible for the decreasing coefficient. Alternatively, the adhesive coefficient may be tied to F_P . It is proposed that the relative roughness of the fracture surface is reduced as nano-scale wear tracks and material transfer takes place to reduce the impact of asperity plowing. Finally, the adhesive friction coefficient values, ranging from 0.25-0.1, are typical but somewhat low for graphitic material in vacuum [30], [35]. It is possible that this is consistent for CVI PyC microstructure, but few friction studies on this exact material were found. TEM and x-ray photoelectron spectroscopy would be excellent techniques to further understand the structural and chemical composition of the tribo-surface that resulted in these values.

4.3 Abrasive friction

During prolonged cycling, wear debris was introduced into the tribo-surface. The mode of particle evolution depended on PyC fatigue for H-thick, pre-existing defects for S-thick, and interacting SiC asperities for H- and S-thin. Regardless of the evolution mode, the abrasive friction values are consistently larger and more turbulent than the adhesive regime. It is easy to understand that contribution from F_p significantly increases as sharp PyC and SiC fragments plow into the interacting surfaces. It is proposed that the initiating debris results in large and random particles that cause transitional regimes with peak friction values. As cycling continues these particles are broken down and smoothened, ejected, or in some cases rolled up. This leads to the steady-state abrasive friction regimes presented in Figure 16B. H-thick and S-thick samples with $h/R_{\max} \gg 1$ showed gradually decreasing friction values. This is attributed to a balance of continuous debris refinement and simultaneous replenishment of asperities from the thick PyC reservoir. As the asperities collectively smooth out and roll up, the rate at which new asperities are formed slows down, leading to the overall coefficient decrease. Another consideration is that the load is applied via set displacement while the interface is continuously losing material, observed in the FIB trenches of Figure 13F. This could result in a time dependent reduction of Z load that is indiscernible from the global load drift of the SmarTip. The decreasing coefficient could therefore be artifact of the test configuration. It is not clear how much influence this has since material removal is likely only tens of nanometers. However, introducing a more robust load cell below the substrate that is resistant to torque loads could solve this problem. It is also noted that the values for S-thick are consistently ≈ 0.2 less than H-thick. Both have $h/R_{\max} \gg 1$, the only difference is fracture location. It is proposed that the lower friction of S-thick is because both interacting surfaces are soft PyC, thereby reducing relative influence from F_p compared to the SiC/PyC interface of H-thick.

Sample H-thin is an example of a test with limited PyC extrusion because $h/R_{\max} \approx 1$. Here it is proposed that SiC fiber asperities are large enough to interact with the SiC matrix, causing local stresses and chipping that quickly break down the PyC bond layer. This leads to third body debris that forms rolled asperities and stabilizes the friction coefficient, shown Figure 16B. Slight increase in friction coefficient over

time is attributed to small amounts of the asperities being removed either at the edge or within the underlying porosity. In this case as the carbon leaves the interface, load redistribution may cause more interaction between the SiC surfaces thereby increasing F_p contribution. However, H-thin shows lower abrasive friction values compared to H-thick. This is attributed to the rapid evolution of rolled asperities that may be the most efficient form of debris to reduce plowing effects. Figure 11C shows significantly larger and more uniform rolled asperities compared to H-thick in Figure 9F.

Raman data correlates the third body particles with significant structural damage in the carbon. Figure 17 shows a pronounced increase in G-FWHM and decrease in both G-peak position and I_D/I_G for all samples after 1000 cycles, suggesting a transition from nano-crystalline sp^2 ring clusters to amorphous carbon chain-like structures. This implies increased dangling bond density available for cold welding, thereby increasing contribution of F_A . Again, it is unlikely that any passivation occurred. Even when the length scale is reduced to an asperity radius of $a = 10$ nm, temperature rise is still negligible at ≈ 0.1 K. As a result, the increased frictional resistance observed in the abrasive regimes is attributed to combined effects of enhanced asperity plowing and adhesion mechanisms. The turbulence suggests plowing effects F_p are dominant.

4.4 Summary and data application

A summary of the interface characteristics, relevant wear mechanisms, and resulting friction as a function of cycle for the steady-state regimes are presented in Table 3. Keep in mind that many samples also expressed transient regimes with large friction coefficients ($\mu_k > 1.5$) before reaching steady-state.

Table 3 – Summary of steady-state tribological behavior

Name	H-thick		H-thin	S-thick	S-thin
h/R_{\max}	~25		~1	~50	~0.5
Fracture location	SiC _f /PyC		SiC _f /PyC*	Within PyC	SiC _f /PyC*
Wear mechanism	Adhesive	Abrasive	Abrasive	Abrasive	Abrasive
Wear debris evolution	None	PyC fatigue	SiC asperity interaction	CVI PyC nodule shatter	SiC asperity interaction
Friction evolution	Decreasing μ by surface smoothing and transfer	Decreasing μ by PyC refinement and rolling	Increasing μ from PyC removal & interacting SiC	Decreasing μ by PyC refinement and rolling	SiC Asperity locking and fiber failure
Raman results	Limited degradation of ring clusters and structure	Significant degradation of the carbon structure; remaining sp ²	Most significant degradation of the carbon structure: remaining sp ²	Significant degradation of the carbon structure; remaining sp ²	Limited degradation and revealed matrix side PyC
Steady-state $\mu_k(N)$	0.26 - 0.0018N	0.77 - 0.00034N	0.36 + 0.00010N	0.51 - 0.00025N	~1.25*

*Estimated

From here, relationships can be explored between the fiber fretting test and composite performance, modelling, and design. In Appendix A, the mini-composite tests of H-thin and S-thin found interfacial sliding stress, τ_s , of 17 MPa and 62 MPa, respectively, based on the micro-crack spacing and estimated residual compressive stress at ≈ 200 MPa [19]. These tests achieved approximately 10 cycles between the onset of matrix cracking and failure. This corresponds to the transitional friction regimes observed for H-thin and S-thin in Figure 10 and Figure 14, with estimated coefficients of 0.8 and 1.25 respectively. With the advantage of user defined compressive stress, σ_o in Table 2, the sliding stress can be calculated as

$$\tau_{fretting} = \mu_k \cdot \sigma_o \quad (6)$$

with average values of ≈ 50 MPa and ≈ 100 MPa found for H-thin and S-thin. While showing the same trend, the property values from micro-crack spacing underestimates the fundamental values from the fretting test.

Additionally, the fretting test provides mechanistic information that can be vital to the development of constituent-based modelling.

Ultimately, the friction data, SEM, and Raman spectroscopy successfully defined a degradation path for the given interface conditions. This is useful for composite design; if interested in fabricating an interface with specific friction coefficient and degradation path, the CVI parameters can be tailored to start at different points on the Raman trajectory, while additionally promoting specific interfacial failure location. From a modelling perspective, the appropriate coefficient and responsible mechanisms can be applied given a known starting structure. The question remains, how well does the fretting test mimic composite scale behavior? Certainly, in the context of confined composite interfaces, there are some attributes that do not align with reality such as segment edge plowing or debris removal. However, it was shown that the fretting test can probe both adhesive sliding and abrasive wear that would be expected for many composite interface conditions. It is also thought that the center of the fiber segment provides reasonable confinement to correlate degradation. Systematic comparisons of fretting and composite tensile tests would authenticate these claims. With that, there are still some physical limitations of the test related to achievable load. Stress concentrations at the gripper-fiber couple (conical or claw) are likely to limit compressive loading to < 100 mN (500 MPa for current segment geometry). Calculations for residual compressive stress in real composites based on thermal mismatch and fiber roughness can easily reach > 1 GPa [19]. However, provided friction mechanisms stay consistent, it may be possible to extrapolate the coefficient based on systematic studies from 0 to 500 MPa.

Overall, the controlled load, indefinite cycle length, frequency, and uniquely accessible tribo-surface for mechanistic insight is thought to outweigh the short comings and provide extremely valuable data. Some recommendations for future experiments and analysis include exhaustive testing with a conical tip. The readily available tips and the self-aligning characteristics make experimental execution much simpler. The initial friction behavior was not ideal, however continued cycling may have led to equivalent probing of the abrasive friction regime. Sensitivity studies evaluating the influence of fiber misalignment under the same

test and interphase conditions could validate several assumptions. A scratch stage with both x-y translation and stub rotation would simplify alignment procedures and enable controlled misalignment studies. Finite element analyses to characterize contact stress concentration and interfacial stress distribution would help refine assumptions regarding projected stress and Coulomb friction. This could also support Hertzian contact models to better characterize PyC fatigue and wear rate. Lastly, the test apparatus is simple enough to explore alternate composite systems and environmental effects provided integration of high temperature and moisture tolerant components. Combined with additional characterization tools such as TEM and XPS, the interfacial modelling and design space can be effectively mapped for myriad composites.


5 Conclusion

A novel fiber fretting test was developed to probe friction properties and tribological mechanisms of continuous fiber composites. Details regarding experimental execution and analysis were laid out explicitly with intention for repeatability and technique advancement. The design was relatively simple, applying existing scratch techniques to a FIB milled surface structure. Four different $\text{SiC}_f/\text{PyC}/\text{SiC}_m$ composite interfaces were evaluated in a SEM vacuum environment. Friction data was accurately extracted and assigned relevant mechanisms based on SEM and Raman spectroscopy characterization. Steady-state friction regimes corresponding to adhesive and abrasive mechanisms were identified and descriptive equations for friction coefficient as a function of cycle were presented. These values were discussed in the context of macroscopic composite behavior to elucidate the potential contributions this test can have for composite modelling and design.

6 Acknowledgements

This work was made possible through the collaborative efforts between UC Berkeley and Swiss Federal Laboratories (Empa, Thun). The first author and corresponding author would like to thank the DOE NEUP program [DE-NE0008460] for student and research support. The first author also wants to thank the Empa funding sources and the ThinkSwiss Scholarship for enabling and supporting this developmental research.

The work would not have been possible without expert guidance from the Alemnis team including Damian Frey and Simeon Bodenmann. Thank you to Dr. Wu's MSE group and Jiaman Liu (PhD) at UC Berkeley for access and operation of their Raman system. Thank you to Amit Sharma (Empa postdoc) for high resolution TEM of the PyC interphase. T.E.J.E. received funding from EMPAPOSTDOCS-II of the European Union's Horizon 2020 research and innovation programme under the Marie Skłodowska-Curie grant agreement

number 754364 . Lastly, we thank the Lawrence Berkeley National Laboratory National Center for Electron Microscopy (LBNL NCEM), Berkeley, CA. Work at the Molecular Foundry was supported by the Office of Science, Office of Basic Energy Sciences, of the U.S. Department of Energy under Contract No. DE-AC02-05CH11231.

7 Appendix A

7.1 Uniaxial tensile testing of mini-composites

Many studies have applied uniaxial tensile testing to correlate composite behavior and constituent level characteristics [1], [3], [16], [55]–[57]. The specific goal of this effort was to compare interface properties from micro- to macro-scale based on micro-crack evolution as it relates to interfacial sliding stress. An analytical model for interfacial sliding stress is related to matrix crack spacing by the following equation [3]

$$\tau_s = \frac{\sigma_s R_f V_m}{2V_f L_s} \quad (A.1)$$

where σ_s is the crack saturation stress (usually taken to be the peak stress before failure for PyC interface containing composites [56]), R_f is the fiber radius, V is the volume fraction for matrix and fiber respectively, and L_s is the average measured crack spacing across the gauge length. Testing in the SEM enabled unique insight into the micro-crack spacing and crack opening, L_o . When the sliding strength is large, the matrix carries more load and will produce shorter crack intervals [15].

Testing was performed using the 500 N Kammrath & Weiss Tensile and Compression Module *in-situ* XL30 Phillips SEM, Figure A.1-A. Uniaxial tension was applied in displacement control at 1 $\mu\text{m/s}$ with prescribed loading and unloading in 5 N steps until failure. Testing was paused periodically to take SEM images of the entire gauge length mid test for insight into crack spacing and crack opening. The mini-composites were cut to ≈ 5 cm long; 2 cm was used for gripping on both ends leaving a 1 cm gauge length. The ends were epoxy mounted in bored and externally threaded studs and set to cure in an alignment fixture, Figure A.1-B. Gauge length restrictions eliminated the option for high precision strain gauges suggested by ASTM standards to guarantee $< 5\%$ bending. To address this, a stainless steel (SS) ball-and-socket gripping system with colloidal graphite lubrication was used to promote self alignment, shown in Figure A.1-A,C.

Figure A.1 – **INSERT (width = 140mm, color online)**

In some samples, the micro-cracking did not evolve perpendicular to the fiber direction. These tests were assumed to be misaligned and discarded. In total, two H-thin and S-thin mini-composites were successful. The area, porosity, fiber radius, and fiber volume fraction were extracted for each mini-composite from fracture surface cross-sections as shown in Figure A.1-D, and are listed in Table A.1. Figure A.1-E shows a typical stress-strain curve from which average proportional limit stresses (PLS) and ultimate tensile strength (UTS) were extracted and tabulated below. The lower PLS value of S-thin is attributed to relative increase in porosity as it relates to critical defect distribution. The ultimate tensile strength was on average about 300 MPa for both. These values align reasonably well with literature⁴³. The crack opening, crack spacing, and corresponding τ_s are pictured in Figures A.1-E,F and listed in Table A.1. The difference in τ_s of the two composites is attributed to the h/R_{max} ratio, representing the degree of asperity interaction between the fiber and matrix.¹⁹ Composite S-thin has ratio 0.5 compared to 1 of H-thin, which resulted in

an increased friction resistance (also found in fretting test). This reduces the debond length and increases the load shared by the matrix, leading to increased micro-crack density.

Table A.1 – Mini-composite tensile test characteristics

Characteristic	H-thin	S-thin
Area (mm ²)	0.25	0.52
Porosity (%)	4	8
V _f (%)	25	25
Avg. fiber radius (μm)	6.5	5.3
h/R_{\max}	1	0.5
σ_R (MPa) [19]	190	210
PLS (MPa)	175	125
UTS (MPa)	305	315
L_s (μm)	185	110
τ_s (MPa)	17	62
Avg. L_o (μm)	2	2

8 References

- [1] A. G. Evans and F. W. Zok, "The physics and mechanics of fibre-reinforced brittle matrix composites," *J. Mater. Sci.*, vol. 29, no. 15, pp. 3857–3896, 1994, doi: 10.1007/BF00355946.
- [2] W. A. Curtin, B. K. Ahn, and N. Takeda, "Modeling brittle and tough stress-strain behavior in unidirectional ceramic matrix composites," *Acta Mater.*, vol. 46, no. 10, pp. 3409–3420, 1998, doi: 10.1016/S1359-6454(98)00041-X.
- [3] N. P. Bansal and J. Lamon, *Ceramic Matrix Composites: Materials, Modeling and Technology*, vol. 9781118231. John Wiley and Sons, 2014.
- [4] A. G. Evans, F. W. Zok, and R. M. McMeeking, "Fatigue of ceramic matrix composites," *Acta Metall. Mater.*, vol. 43, no. 3, pp. 859–875, 1995, doi: 10.1016/0956-7151(94)00304-Z.
- [5] L. Longbiao, "Modeling matrix cracking of fiber-reinforced ceramic-matrix composites under oxidation environment at elevated temperature," *Theor. Appl. Fract. Mech.*, vol. 87, pp. 110–119, 2017, doi: 10.1016/j.tafmec.2016.11.003.
- [6] L. Longbiao, "Micromechanical modeling of fatigue hysteresis behavior in carbon fiber-reinforced ceramic-matrix composites. Part I: Theoretical analysis," *Compos. Part B Eng.*, vol. 159, pp. 502–513, Feb. 2019, doi: 10.1016/j.compositesb.2014.09.036.
- [7] W. A. Curtin, "Stochastic Damage Evolution and Failure in Fibre-Reinforced Composites," *Adv. Appl. Mech.*, vol. 36, pp. 164–248, 1999, doi: [https://doi.org/10.1016/S0065-2156\(08\)70186-8](https://doi.org/10.1016/S0065-2156(08)70186-8).
- [8] R. J. Kerans and R. S. Hay, "Interface Design for Oxidation-Resistant Ceramic Composites," *J. Am.*

Ceram. Soc., vol. 85, pp. 2599–2632, 2002, doi: 10.1111/j.1151-2916.2002.tb00505.x.

- [9] S. Pasquier, J. Lamon, and R. Naslain, “Tensile static fatigue of 2D SiC/SiC composites with multilayered (PyC-SiC)_n interphases at high temperatures in oxidizing atmosphere,” *Compos. Part A Appl. Sci. Manuf.*, vol. 29, no. 9–10, pp. 1157–1164, Jan. 1998, doi: 10.1016/S1359-835X(98)00093-1.
- [10] C. H. Hsueh, F. Rebillat, J. Lamon, and E. Lara-Curzio, “Analyses of fiber push-out tests performed on Nicalon/SiC composites with tailored interfaces,” *Compos. Eng.*, vol. 5, no. 10–11, pp. 1387–1401, 1995, doi: 10.1016/0961-9526(95)99801-A.
- [11] W. M. Mueller, J. Moosburger-Will, M. G. R. Sause, and S. Horn, “Microscopic analysis of single-fiber push-out tests on ceramic matrix composites performed with Berkovich and flat-end indenter and evaluation of interfacial fracture toughness,” *J. Eur. Ceram. Soc.*, vol. 33, no. 2, pp. 441–451, 2013, doi: 10.1016/j.jeurceramsoc.2012.09.009.
- [12] S. Bertrand, R. Pailler, and J. Lamon, “Influence of strong fiber/coating interfaces on the mechanical behavior and lifetime of Hi-Nicalon/(PyC/SiC)_n/SiC minicomposites,” *J. Am. Ceram. Soc.*, vol. 84, no. 4, pp. 787–794, 2001, doi: 10.1111/j.1151-2916.2001.tb00742.x.
- [13] A. Hussey, R. De Meyere, C. Deck, D. E. J. Armstrong, and Y. Zayachuk, “Statistically sound application of fiber push-out method for the study of locally non-uniform interfacial properties of SiC-SiC fiber composites,” *J. Eur. Ceram. Soc.*, vol. 40, no. 4, pp. 1052–1056, Apr. 2020, doi: 10.1016/j.jeurceramsoc.2019.11.041.
- [14] J. Kabel *et al.*, “Micro-Mechanical Evaluation of SiC-SiC Composite Interphase Properties and Debond Mechanisms,” *Compos. Part B Eng.*, vol. 131, pp. 1–18, 2017, doi: 10.1016/j.compositesb.2017.07.035.
- [15] J. Kabel *et al.*, “Ceramic composites: A review of toughening mechanisms and demonstration of micropillar compression for interface property extraction,” *J. Mater. Res.*, vol. 33, no. 4, pp. 424–439, Feb. 2018, doi: 10.1557/jmr.2017.473.
- [16] E. Vagaggini, J. -M Domergue, and A. G. Evans, “Relationships between Hysteresis Measurements and the Constituent Properties of Ceramic Matrix Composites: I, Theory,” *Journal of the American Ceramic Society*, vol. 78, no. 10, pp. 2709–2720, 1995, doi: 10.1111/j.1151-2916.1995.tb08046.x.
- [17] Y. Katoh, L. L. Snead, T. Nozawa, S. Kondo, and J. T. Busby, “Thermophysical and Mechanical Properties of Near-stoichiometric Fiber CVI SiC/SiC Composites after Neutron Irradiation at Elevated Temperatures,” *J. Nucl. Mater.*, vol. 403, no. 1–3, pp. 48–61, 2010, doi: 10.1016/j.jnucmat.2010.06.002.
- [18] E. Buet, C. Sauder, D. Sornin, S. Poissonnet, J. Rouzaud, and C. Vix-guterl, “Influence of surface fibre properties and textural organization of a pyrocarbon interphase on the interfacial shear stress of SiC / SiC minicomposites reinforced with Hi-Nicalon S and Tyranno SA3 fibres,” *J. Eur. Ceram. Soc.*, vol. 34, no. 2, pp. 179–188, 2014, doi: 10.1016/j.jeurceramsoc.2013.08.027.
- [19] C. Sauder, A. Brusson, and J. Lamon, “Influence of interface characteristics on the mechanical properties of Hi-nicalon type-S or tyranno-SA3 fiber-reinforced SiC/SiC minicomposites,” *Int. J. Appl. Ceram. Technol.*, vol. 7, no. 3, pp. 291–303, 2010, doi: 10.1111/j.1744-7402.2010.02485.x.
- [20] D. Casari *et al.*, “A self-aligning microtensile setup: Application to single-crystal GaAs microscale tension–compression asymmetry,” *J. Mater. Res.*, pp. 1–18, Jun. 2019, doi: 10.1557/jmr.2019.183.
- [21] G. Dehm, B. N. Jaya, R. Raghavan, and C. Kirchlechner, “Acta Materialia Overview on micro- and nanomechanical testing : New insights in interface plasticity and fracture at small length scales,”

Acta Mater., vol. 142, pp. 248–282, 2018, doi: 10.1016/j.actamat.2017.06.019.

- [22] D. Frazer *et al.*, “Localized mechanical property assessment of SiC/SiC composite materials,” *Compos. Part A Appl. Sci. Manuf.*, vol. 70, pp. 93–101, 2015, doi: 10.1016/j.compositesa.2014.11.008.
- [23] M. Sebastiani, C. Eberl, E. Bemporad, and G. M. Pharr, “Depth-resolved residual stress analysis of thin coatings by a new FIB-DIC method,” *Mater. Sci. Eng. A*, vol. 528, no. 27, pp. 7901–7908, Oct. 2011, doi: 10.1016/j.msea.2011.07.001.
- [24] D. K. Shetty, “Shear-Lag Analysis of Fiber Push-Out (Indentation) Tests for Estimating Interfacial Friction Stress in Ceramic-Matrix Composites,” *J. Am. Ceram. Soc.*, vol. 71, no. 107, 1988, doi: 10.1111/j.1151-2916.1988.tb05843.x.
- [25] F. Bowden, F. Bowden, and D. Tabor, *The friction and lubrication of solids*, vol. 1. Oxford University Press, 2001.
- [26] E. Rabinowicz, *Friction and Wear of Materials (2nd Edition)*, 2nd ed. New York: John Wiley & Sons, 1995.
- [27] B. Bhushan, *Modern Tribology Handbook*, 1st ed., vol. 1 & 2. Boca Raton: CRC Press LLC, 2001.
- [28] S. Lafon-Placette *et al.*, “Tribological characterization of silicon carbide and carbon materials,” *J. Eur. Ceram. Soc.*, vol. 35, no. 4, 2014, doi: 10.1016/j.jeurceramsoc.2014.10.038i.
- [29] S. K. Sharma, B. V. M. Kumar, and Y. W. Kim, “Tribological behavior of silicon carbide ceramics - A review,” *Journal of the Korean Ceramic Society*, vol. 53, no. 6. Korean Ceramic Society, pp. 581–596, Nov. 01, 2016, doi: 10.4191/kcers.2016.53.6.581.
- [30] J. Xiao, L. Zhang, K. Zhou, J. Li, X. Xie, and Z. Li, “Anisotropic friction behaviour of highly oriented pyrolytic graphite,” *Carbon N. Y.*, vol. 65, pp. 53–62, Dec. 2013, doi: 10.1016/j.carbon.2013.07.101.
- [31] X. Luo, X. Li, and S. Yu, “Nuclear graphite friction properties and the influence of friction properties on the pebble bed,” in *Nuclear Engineering and Design*, Oct. 2010, vol. 240, no. 10, pp. 2674–2681, doi: 10.1016/j.nucengdes.2010.07.030.
- [32] D. W. Kim and K. W. Kim, “Effects of sliding velocity and normal load on friction and wear characteristics of multi-layered diamond-like carbon (DLC) coating prepared by reactive sputtering,” *Wear*, vol. 297, no. 1–2, pp. 722–730, Jan. 2013, doi: 10.1016/j.wear.2012.10.009.
- [33] B. K. Yen, “Roles of oxygen in lubrication and wear of graphite in “dusting” and ambient conditions,” *J. Mater. Sci. Lett.*, vol. 14, no. 21, pp. 1481–1483, 1995, doi: 10.1007/BF00633136.
- [34] T. Xing *et al.*, “Disorder in ball-milled graphite revealed by Raman spectroscopy,” *Carbon N. Y.*, vol. 57, pp. 515–519, Jun. 2013, doi: 10.1016/j.carbon.2013.02.029.
- [35] P. J. Bryant, P. L. Gutshall, and L. H. Taylor, “A study of mechanisms of graphite friction and wear,” *Wear*, vol. 7, no. 1, pp. 118–126, 1964, doi: 10.1016/0043-1648(64)90083-3.
- [36] J. Xiao, L. Zhang, K. Zhou, J. Li, X. Xie, and Z. Li, “Anisotropic friction behaviour of highly oriented pyrolytic graphite,” *Carbon N. Y.*, vol. 65, pp. 53–62, Dec. 2013, doi: 10.1016/j.carbon.2013.07.101.
- [37] A. C. Ferrari and J. Robertson, “Resonant Raman spectroscopy of disordered, amorphous, and diamondlike carbon,” *Phys. Rev. B - Condens. Matter Mater. Phys.*, vol. 64, no. 7, p. 075414, Jul. 2001, doi: 10.1103/PhysRevB.64.075414.

- [38] P. K. Chu and L. Li, "Characterization of amorphous and nanocrystalline carbon films," *Mater. Chem. Phys.*, vol. 96, no. 2–3, pp. 253–277, Apr. 2006, doi: 10.1016/j.matchemphys.2005.07.048.
- [39] A. C. Ferrari and J. Robertson, "Interpretation of Raman spectra of disordered and amorphous carbon," *Phys. Rev. B*, vol. 61, no. 20, May 2000, Accessed: May 06, 2020. [Online]. Available: <https://link.aps.org/doi/10.1103/PhysRevB.61.14095>.
- [40] M. A. Pimenta, G. Dresselhaus, M. S. Dresselhaus, L. G. Cancado, A. Jorio, and R. Saito, "Studying disorder in graphite-based systems by Raman spectroscopy," *Phys. Chem. Chem. Phys.*, vol. 9, pp. 1276–1291, 2007, doi: 10.1039/b613962k.
- [41] F. Rose *et al.*, "Complete characterization by Raman spectroscopy of the structural properties of thin hydrogenated diamond-like carbon films exposed to rapid thermal annealing," *J. Appl. Phys.*, vol. 116, no. 12, p. 123516, Sep. 2014, doi: 10.1063/1.4896838.
- [42] D. Schwallier, B. Clauß, and M. R. Buchmeiser, "Ceramic filament fibers - A review," *Macromolecular Materials and Engineering*, vol. 297, no. 6. John Wiley & Sons, Ltd, pp. 502–522, Jun. 01, 2012, doi: 10.1002/mame.201100364.
- [43] Y. Katoh *et al.*, "Continuous SiC fiber, CVI SiC matrix composites for nuclear applications: Properties and irradiation effects," *J. Nucl. Mater.*, vol. 448, no. 1–3, pp. 448–476, 2014, doi: 10.1016/j.jnucmat.2013.06.040.
- [44] S. Bertrand, C. Droillard, R. Pailler, X. Bourrat, and R. Naslain, "TEM structure of (PyC / SiC) n multilayered interphases in SiC / SiC composites," *J. Eur. Ceram. Soc.*, vol. 20, pp. 1–13, 2000, doi: [https://doi.org/10.1016/S0955-2219\(99\)00086-2](https://doi.org/10.1016/S0955-2219(99)00086-2).
- [45] E. López-Honorato, P. J. Meadows, and P. Xiao, "Fluidized bed chemical vapor deposition of pyrolytic carbon - I. Effect of deposition conditions on microstructure," *Carbon N. Y.*, vol. 47, no. 2, pp. 396–410, Feb. 2009, doi: 10.1016/j.carbon.2008.10.023.
- [46] J. Schindelin *et al.*, "Fiji: An open-source platform for biological-image analysis," *Nature Methods*, vol. 9, no. 7. Nature Publishing Group, pp. 676–682, Jul. 28, 2012, doi: 10.1038/nmeth.2019.
- [47] N. I. Kato, "Reducing focused ion beam damage to transmission electron microscopy samples," *Japanese Soc. Microsc.*, vol. 53, no. 3, pp. 451–458, 2004, doi: 10.1093/jmicro/dfh080.
- [48] K. Thompson, D. Lawrence, D. J. Larson, J. D. Olson, T. F. Kelly, and B. Gorman, "In situ site-specific specimen preparation for atom probe tomography," *Ultramicroscopy*, vol. 107, no. 2–3, pp. 131–139, Feb. 2007, doi: 10.1016/j.ultramic.2006.06.008.
- [49] S. Bertrand, F. Philippe, R. Pailler, and L. Jacques, "Hi-Nicalon/SiC Minicomposites with (Pyrocarbon/SiC) nanoscale multilayered interphases," *J. Am. Ceram. Soc.*, vol. 82, no. 9, pp. 2465–73, 1999, doi: 10.1111/j.1151-2916.1999.tb02105.x.
- [50] Y. Zayachuk, P. Karamched, C. Deck, P. Hosemann, and D. E. J. Armstrong, "Linking microstructure and local mechanical properties in SiC-SiC fiber composite using micromechanical testing," *Acta Mater.*, vol. 168, pp. 178–189, Apr. 2019, doi: 10.1016/j.actamat.2019.02.001.
- [51] K. Johnson, *Contact Mechanics*, 1st ed. Cambridge: Cambridge University Press, 1985.
- [52] F. Rose *et al.*, "Complete characterization by Raman spectroscopy of the structural properties of thin hydrogenated diamond-like carbon films exposed to rapid thermal annealing," *J. Appl. Phys.*, vol. 116, no. 12, p. 123516, Sep. 2014, doi: 10.1063/1.4896838.
- [53] J. Schwan, S. Ulrich, V. Batori, H. Ehrhardt, and S. R. P. Silva, "Raman spectroscopy on amorphous

carbon films," *J. Appl. Phys.*, vol. 80, no. 1, pp. 440–447, Jul. 1996, doi: 10.1063/1.362745.

- [54] A. C. Ferrari and J. Robertson, "Raman spectroscopy of amorphous, nanostructured, diamond-like carbon, and nanodiamond," *Philos. Trans. R. Soc. London. Ser. A Math. Phys. Eng. Sci.*, vol. 362, no. 1824, pp. 2477–2512, Nov. 2004, doi: 10.1098/rsta.2004.1452.
- [55] W. A. Curtin, "Theory of Mechanical Properties of Ceramic-Matrix Composites," *J. Am. Ceram. Soc.*, vol. 74, no. 11, pp. 2837–2845, 1991, doi: 10.1111/j.1151-2916.1991.tb06852.x.
- [56] J. M. Domergue, E. Vagaggini, and A. G. Evans, "Relationships between Hysteresis Measurements and the Constituent Properties of Ceramic Matrix Composites: II, Experimental Studies on Unidirectional Materials," *Journal of the American Ceramic Society*, vol. 78, no. 10, pp. 2721–2731, 1995, doi: 10.1111/j.1151-2916.1995.tb08047.x.
- [57] R. J. Kerans, T. A. Parthasarathy, F. Rebillat, and J. Lamon, "Interface properties in high-strength nicalon/C/SiC composites, as determined by rough surface analysis of fiber push-out tests," *J. Am. Ceram. Soc.*, vol. 81, no. 7, pp. 1881–1887, 1998, doi: <https://doi.org/10.1111/j.1151-2916.1998.tb02561.x>.

9 Figure Captions

Figure 1 – Schematic of fiber fretting test configuration and load distribution considerations.

Figure 2 – TEM micrographs of the fibers and PyC. A) PyC interface with HNLS fiber and overlaid surface trace used for roughness calculations. B) PyC interface with S fiber and overlaid surface trace. C) High resolution TEM of PyC far away from the fiber surface showing PyC (002) lattice fringes (Image C courtesy of Amit Sharma Empa Swiss federal laboratories). D) FFT of HRTEM lattice fringes showing O.A. ~49 corresponding to high texture.

Figure 3 – A) Typical polished composite cross-section with exposed fiber. B) Top-down view of H-thick micro-sliders that were batch milled with the FIB. Sliders 1-3 were originally given center holes for proof of concept conical tip testing. C) Series of images showing the transverse FIB cross-section of all four composite micro-sliders with semi-cylinder geometry.

Figure 4 – A) SEM image of the conical tip gripper with overlaid representation of the piezo sensors in the SmarTip B) SEM images of the claw gripper from the front and side. C) Alemnis scratch system set up in the SEM chamber with overlaid text identifying important components.

Figure 5 – Raman spectrum acquisition and double Lorentzian fit. The SEM images shows the pristine fracture surface and blue laser mark denoting scan location.

Figure 6 – SEM images from in-situ test videos showing the test sequence (vertical progression) for the conical tip (left) and claw tip (right): (1) Initial loading, (2) substrate motion right, (3) substrate motion left, and (4) end of test. Yellow arrows represent the applied displacements. Red lines highlight segment tilting brought on by the conical tip-to-slider couple. The right-hand sequence highlights segment stability enabled by the claw gripper. The lateral displacement frames are from the 10th cycle and show early onset of wear products in the conical tip test.

Figure 7 – Data output and analysis for the friction coefficient. A) Raw data with global load drift. Asymmetric least squares fit (green) for baseline subtraction. B) Adjusted data with displacement, P_x , P_{max} ,

and μ_k . C) Zoom-window near cycle 10 showing shape of steady-state sliding region and overlaid friction envelopes as solid and dashed black lines.

Figure 8 – Friction data for all H-thick composite micro-sliders. A transition from adhesive to abrasive friction is observed with increasing cycle number. No dependence on frequency is observed.

Figure 9 – A-F) SEM images of all H-thick tribo-surfaces. Smooth surfaces suggest adhesive friction mechanisms. Rough surfaces with third body debris suggests a transition to abrasive friction. F) H-thick-6 shows ejected PyC fragments at the corner edges and rolled third body particles at the center. G) Raman spectra of all six samples with clear peak broadening of the 1000 cycle samples.

Figure 10 – Friction data for all H-thin composite micro-sliders at 1Hz. The first 100 cycles show relatively high values with some erratic behavior that decay to a steady-state regime.

Figure 11 – SEM images of all H-thin tribo-surfaces. Progressive rolled third body particle evolution is observed from 10 to 1000 cycles D) Raman spectra showing increased intensity from underlying SiC and clear degradation of the carbon material after 1000 cycles.

Figure 12 - Friction data for all S-thick composite micro-sliders.

Figure 13 – A,B) Reference PyC fracture surface showing pre-existing CVI nodule defects. C-F) SEM images of S-thick tribo-surfaces. Wear debris is observed for all cases. G) Raman spectra show peak broadening with increased cycles.

Figure 14 – Friction data for the first 20 cycles of S-thin composite micro-sliders. Locking and failure events are highlighted based on video evidence.

Figure 15 – A,B) S-thin-1 before and after the segment was removed to reveal the tribo-surface. Fragmentation of the fiber segment as well as underlying porosity are observed. C) Shows a S-thin segment that did not displace. Scratch marks are observed at the gripper/segment contact D,E) S-thin-2 before and after images showing the segment fragmentation and tribo-surface. F) Shows the underside of the S-thin-2 segment after it was removed with evidence of PyC rolling.

Figure 16 – A) Average steady-state kinetic friction coefficient for the adhesive regime observed in composite H-thick B) Steady-state friction coefficients for the adhesive regimes observed in H-thick, H-thin, and S-thick.

Figure 17 – A) Experimental Raman values as a function of cycle for all micro-sliders. B) Ferrari et al. Amorphization trajectory through graphite, nanocrystalline (nc) graphite, amorphous carbon (a-C), and to amorphous tetrahedral carbon (ta-C), reproduced and adapted with permission from ref [39], copyright American Physical Society 2000.

Figure A.1 – A) Kammrath and Weiss module on SEM stage with loaded sample. B) Alignment fixture for epoxy mounting and curing. C) S-thin mini-composite test specimen with SS balls on threaded studs. D) Fracture surface cross-sections of S-thin mini-composites with fiber-pullout visible. E) Stress-strain curves for H-thin. F) S-thin composite with uniform micro-crack spacing across gauge section near UTS. G) High magnification of micro-cracks with overlaid average crack spacing and opening of the S-thin composite.

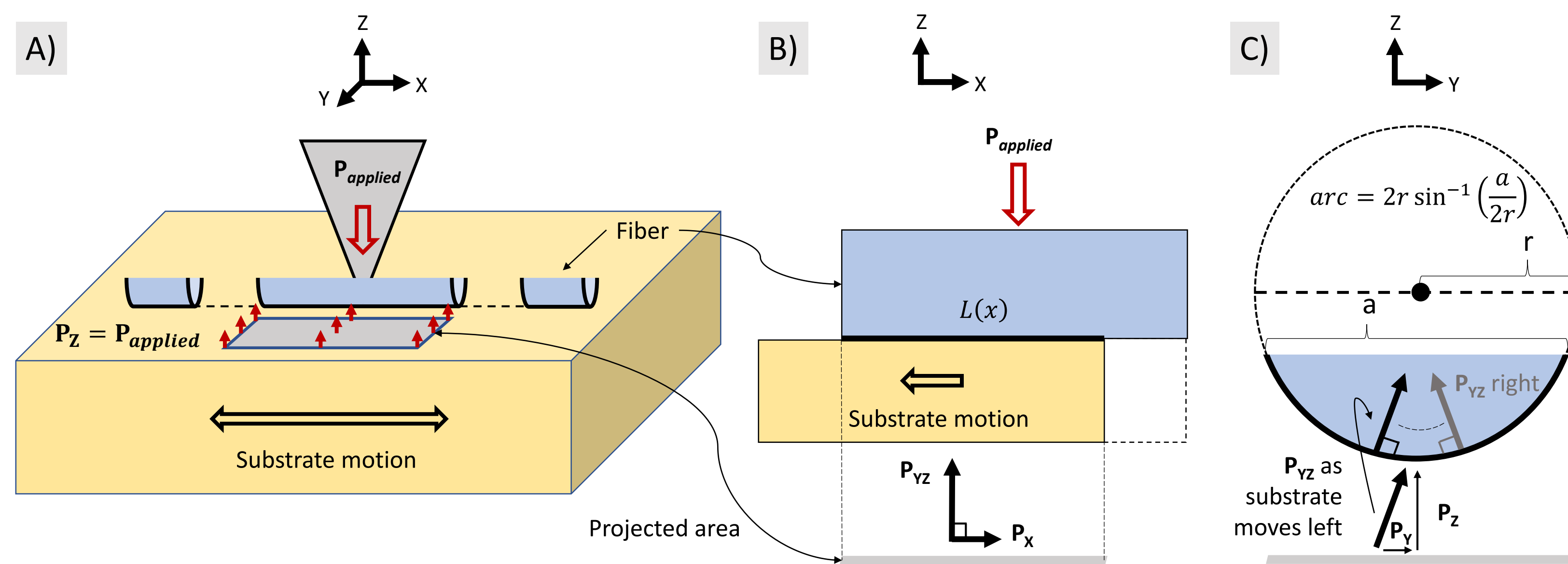


Figure 1 – Schematic of fiber fretting test configuration and load distribution considerations.

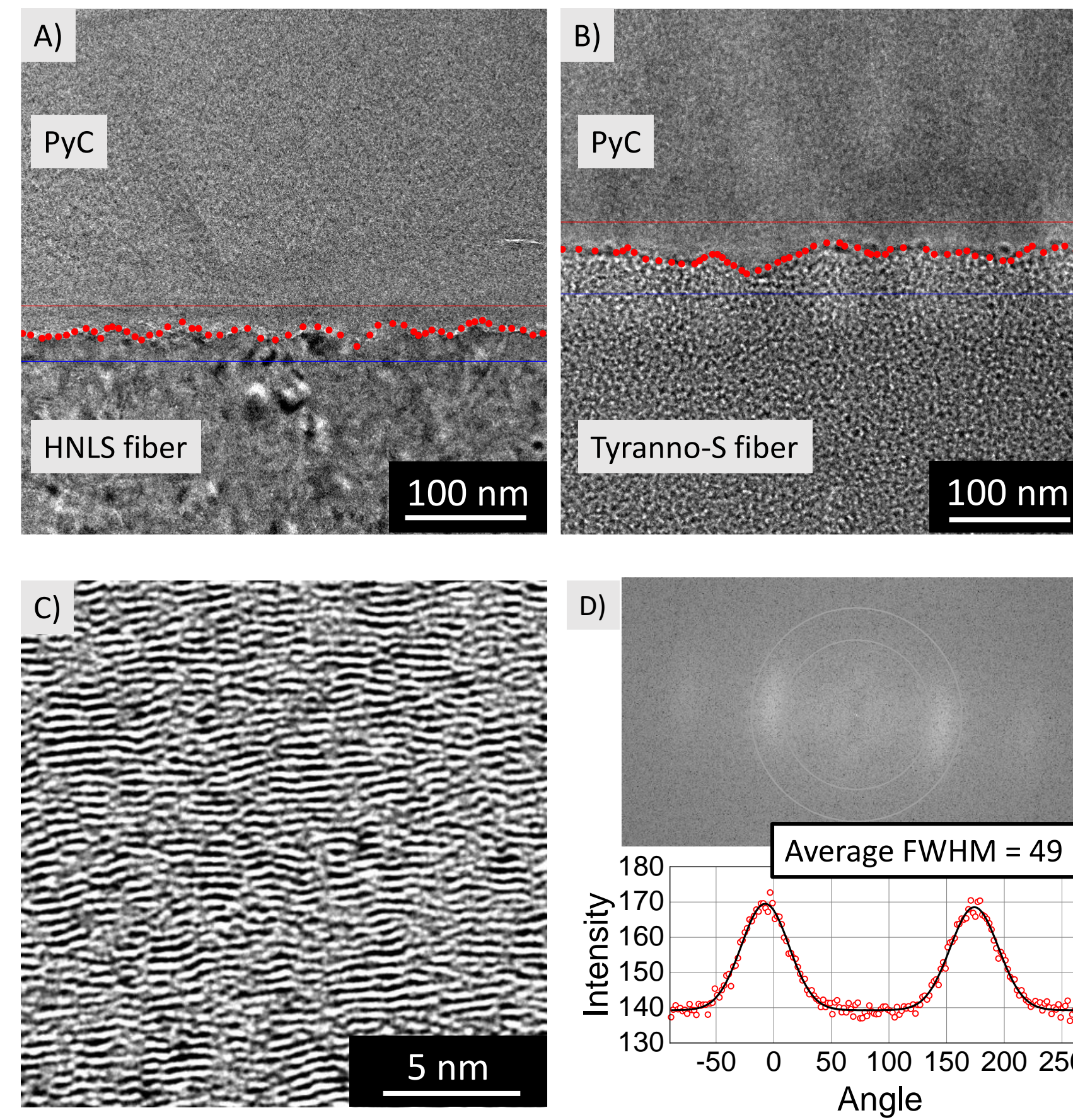


Figure 2 – TEM micrographs of the fibers and PyC. A) PyC interface with HNLS fiber and overlaid surface trace used for roughness calculations. B) PyC interface with S fiber and overlaid surface trace. C) High resolution TEM of PyC far away from the fiber surface showing PyC (002) lattice fringes (Image C courtesy of Amit Sharma Empa Swiss federal laboratories). D) FFT of HRTEM lattice fringes showing O.A. ~ 49 corresponding to high texture.

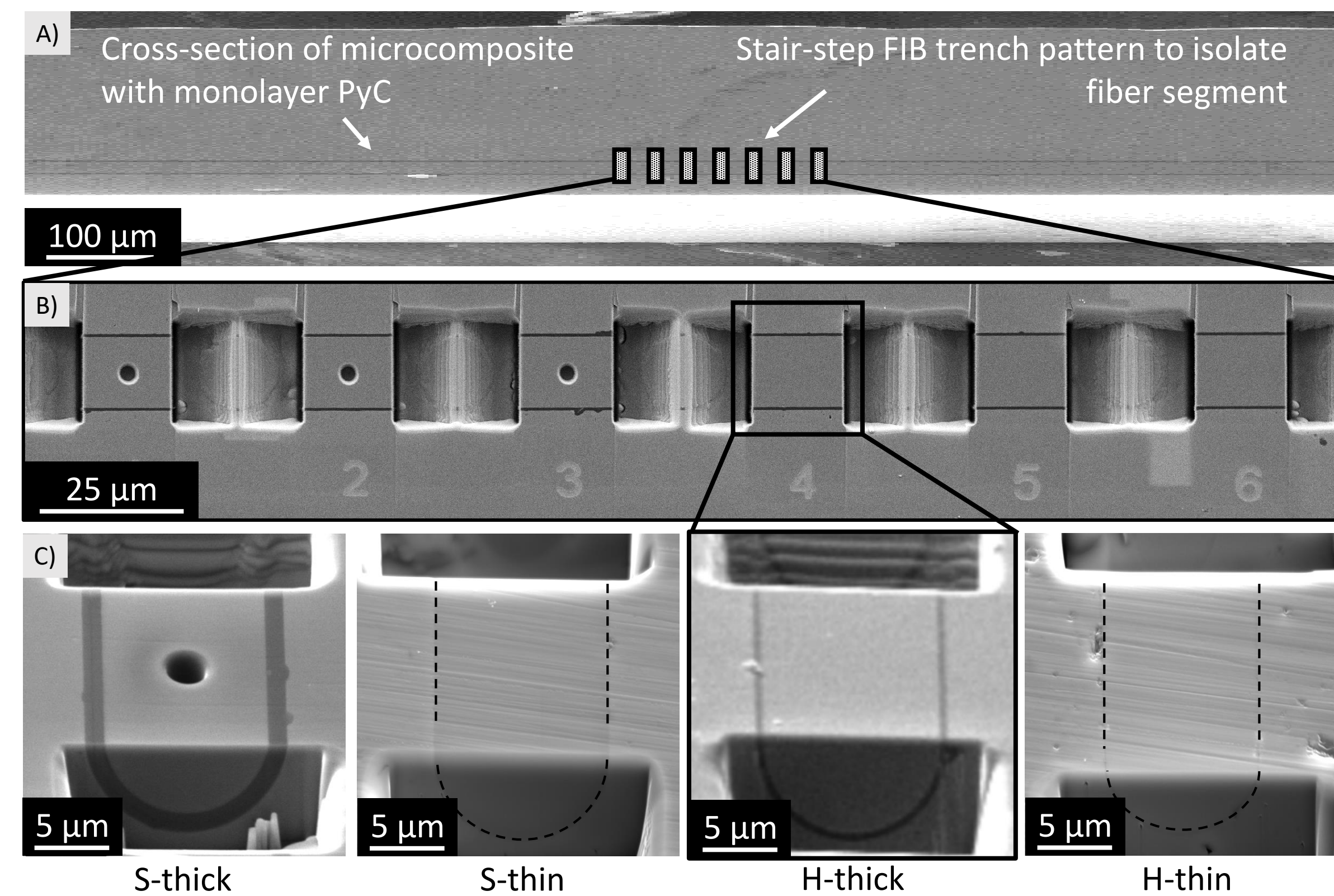


Figure 3 – A) Typical polished composite cross-section with exposed fiber. B) Top-down view of H-thick micro-sliders that were batch milled with the FIB. Sliders 1-3 were originally given center holes for proof of concept conical tip testing. C) Series of images showing the transverse FIB cross-section of all four composite micro-sliders with semi-cylinder geometry.

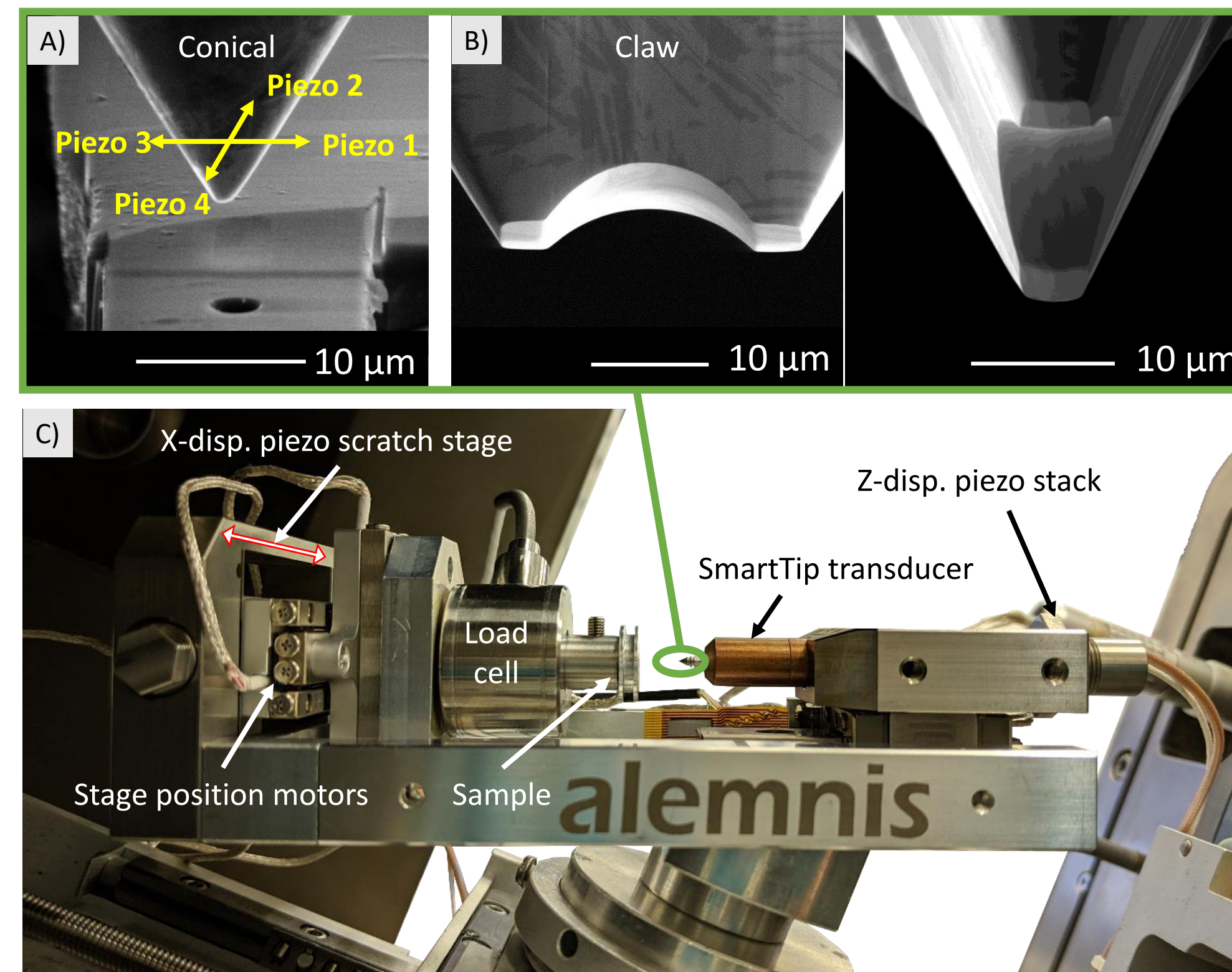


Figure 4 – A) SEM image of the conical tip gripper with overlaid representation of the piezo sensors in the SmartTip B) SEM images of the claw gripper from the front and side. C) Alemnis scratch system set up in the SEM chamber with overlaid text identifying important components.

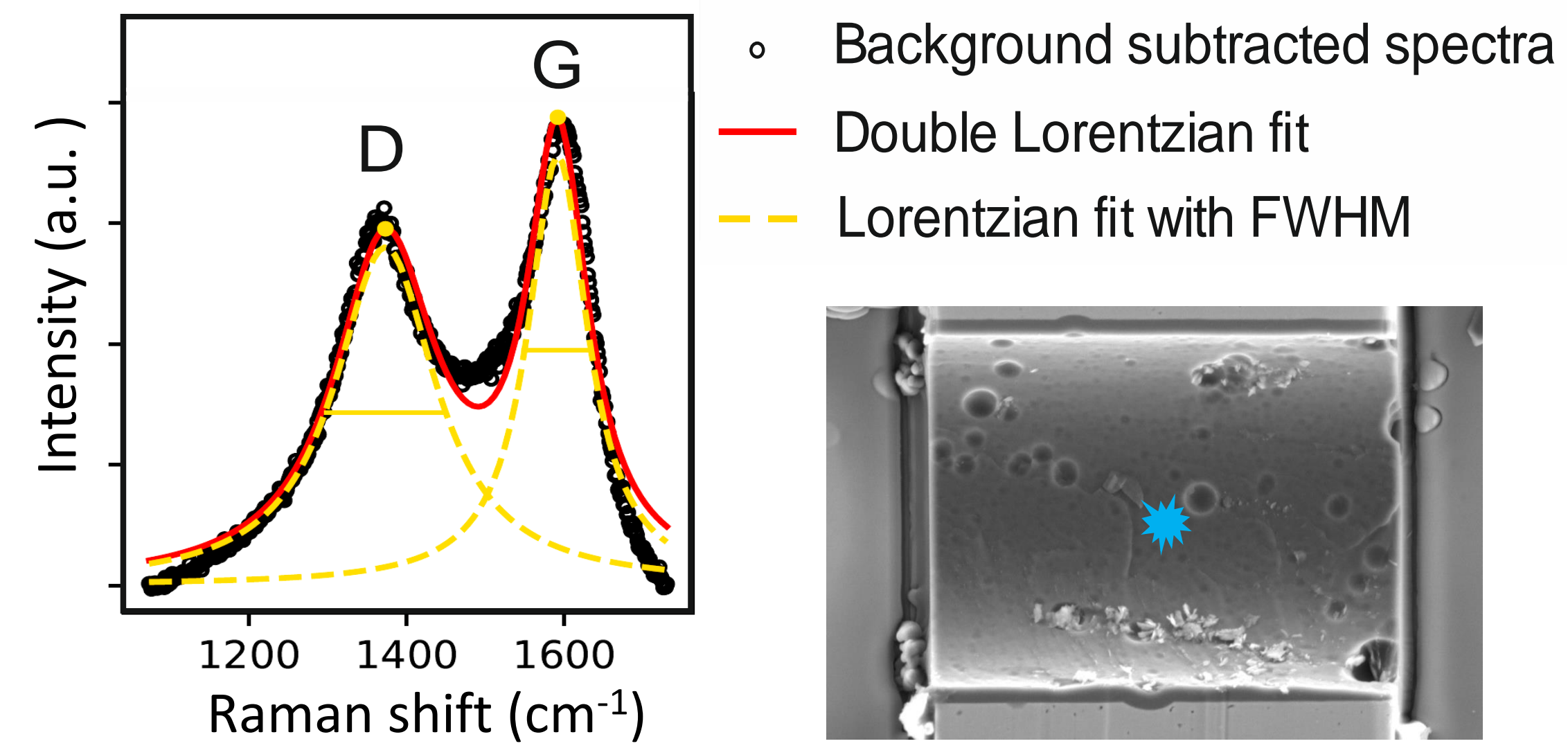


Figure 5 – Raman spectrum acquisition and double Lorentzian fit. The SEM images shows the pristine fracture surface and blue laser mark denoting scan location.

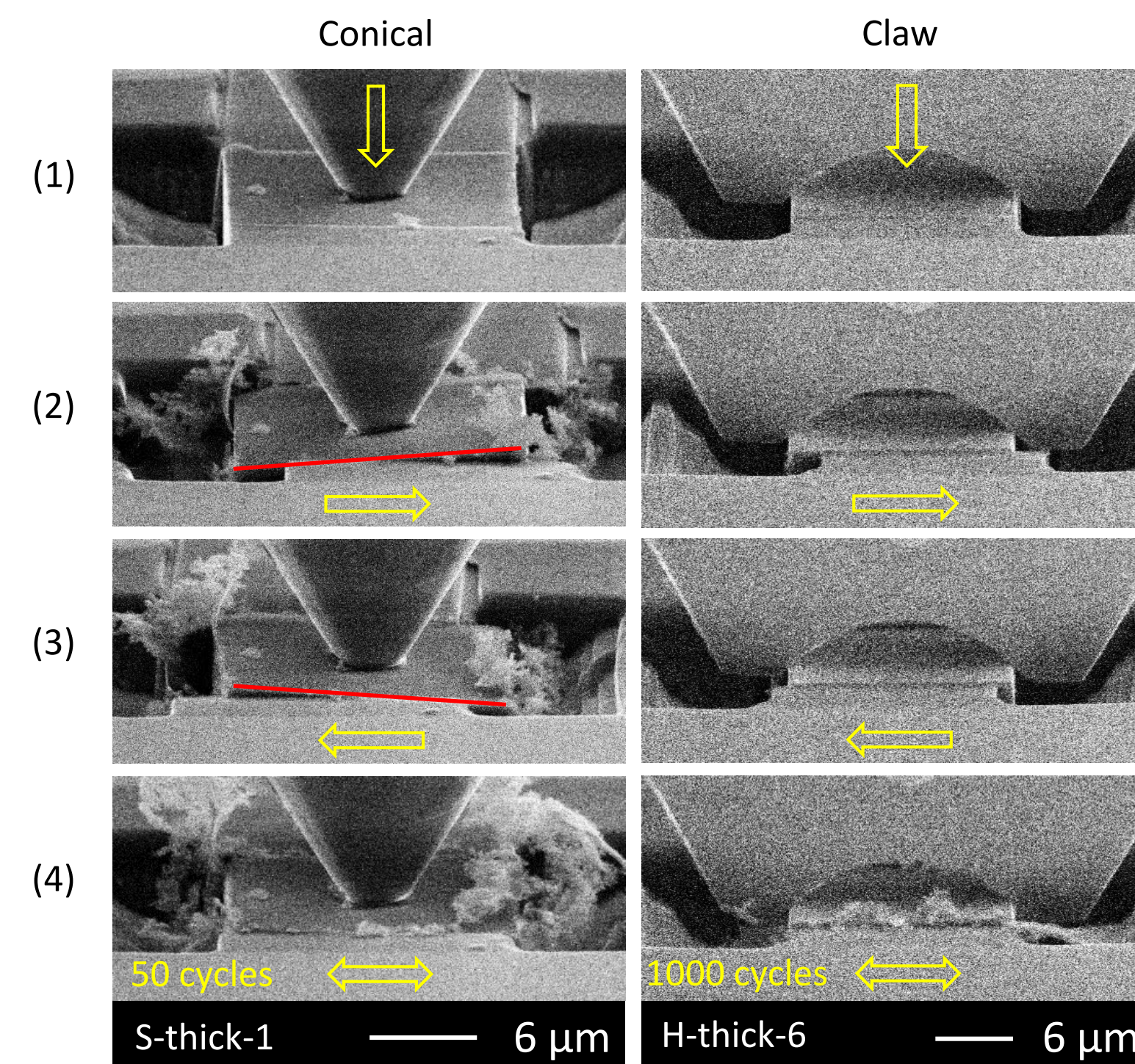


Figure 6 – SEM images from in-situ test videos showing the test sequence (vertical progression) for the conical tip (left) and claw tip (right): (1) Initial loading, (2) substrate motion right, (3) substrate motion left, and (4) end of test. Yellow arrows represent the applied displacements. Red lines highlight segment tilting brought on by the conical tip-to-slider couple. The right-hand sequence highlights segment stability enabled by the claw gripper. The lateral displacement frames are from the 10th cycle and show early onset of wear products in the conical tip test.

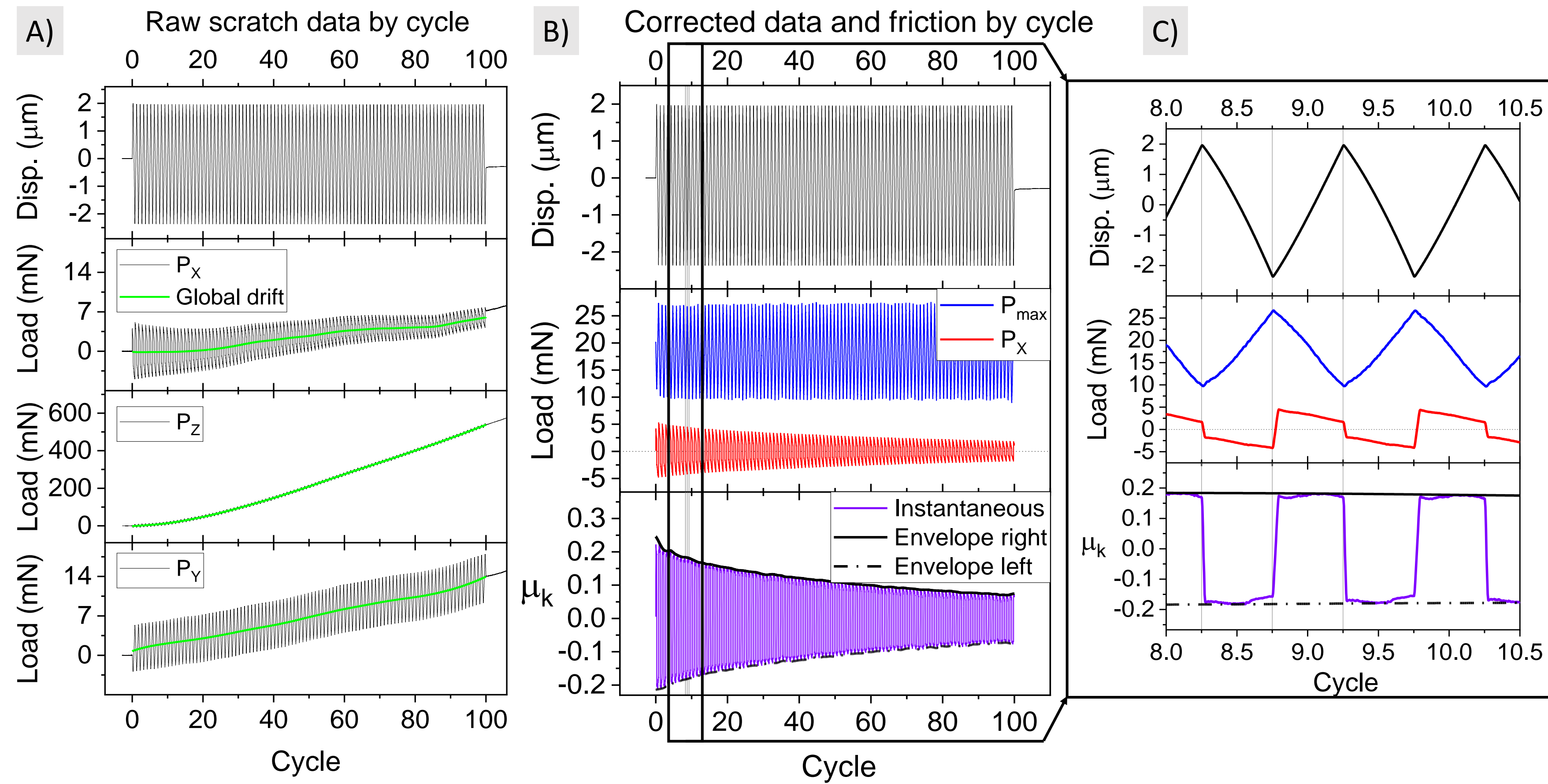


Figure 7 – Data output and analysis for the friction coefficient. A) Raw data with global load drift. Asymmetric least squares fit (green) for baseline subtraction. B) Adjusted data with displacement, P_x , P_{\max} , and μ_k . C) Zoom-window near cycle 10 showing shape of steady-state sliding region and overlaid friction envelopes as solid and dashed black lines.

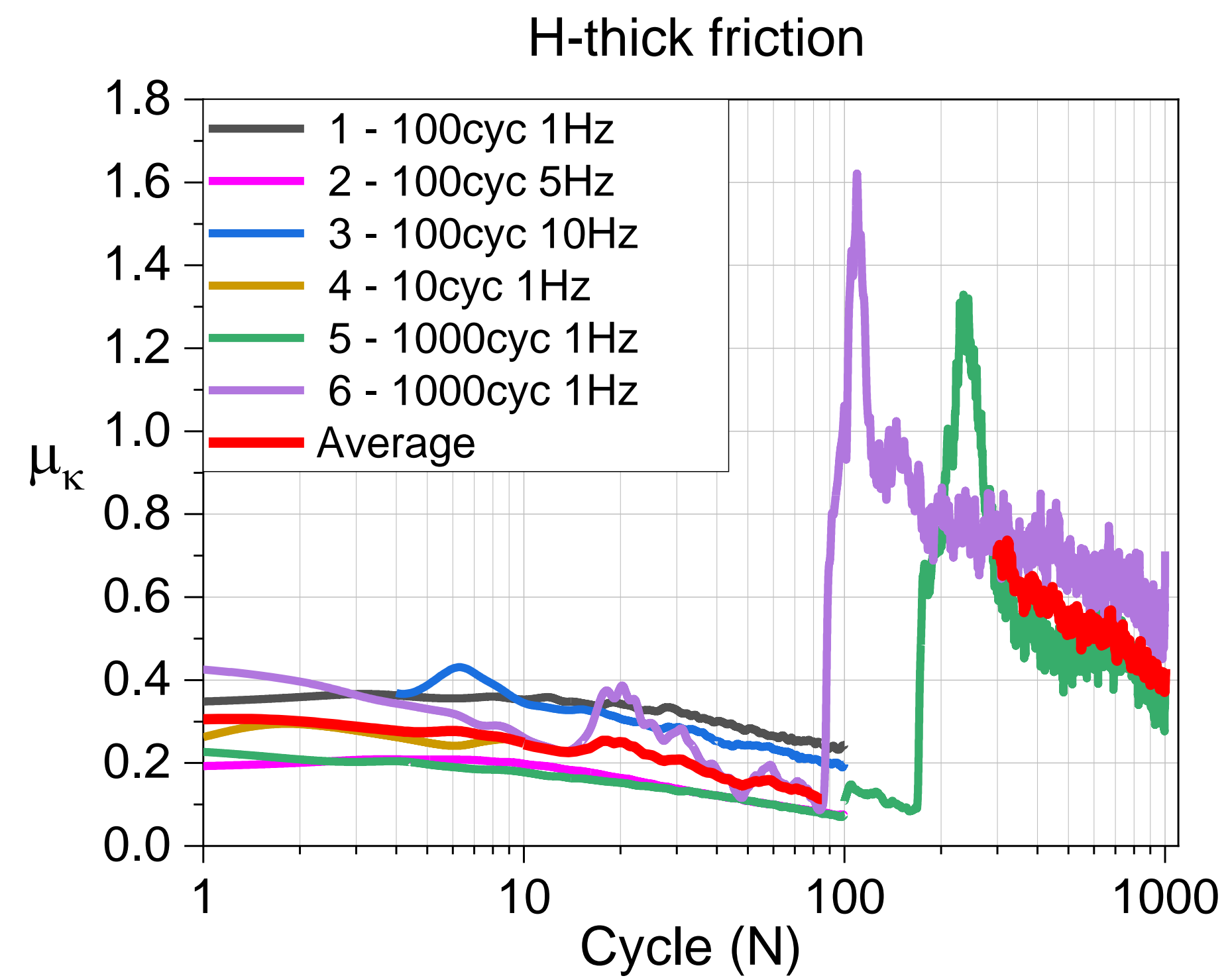


Figure 8 – Friction data for all H-thick composite micro-sliders. A transition from adhesive to abrasive friction is observed with increasing cycle number. No dependence on frequency is observed.

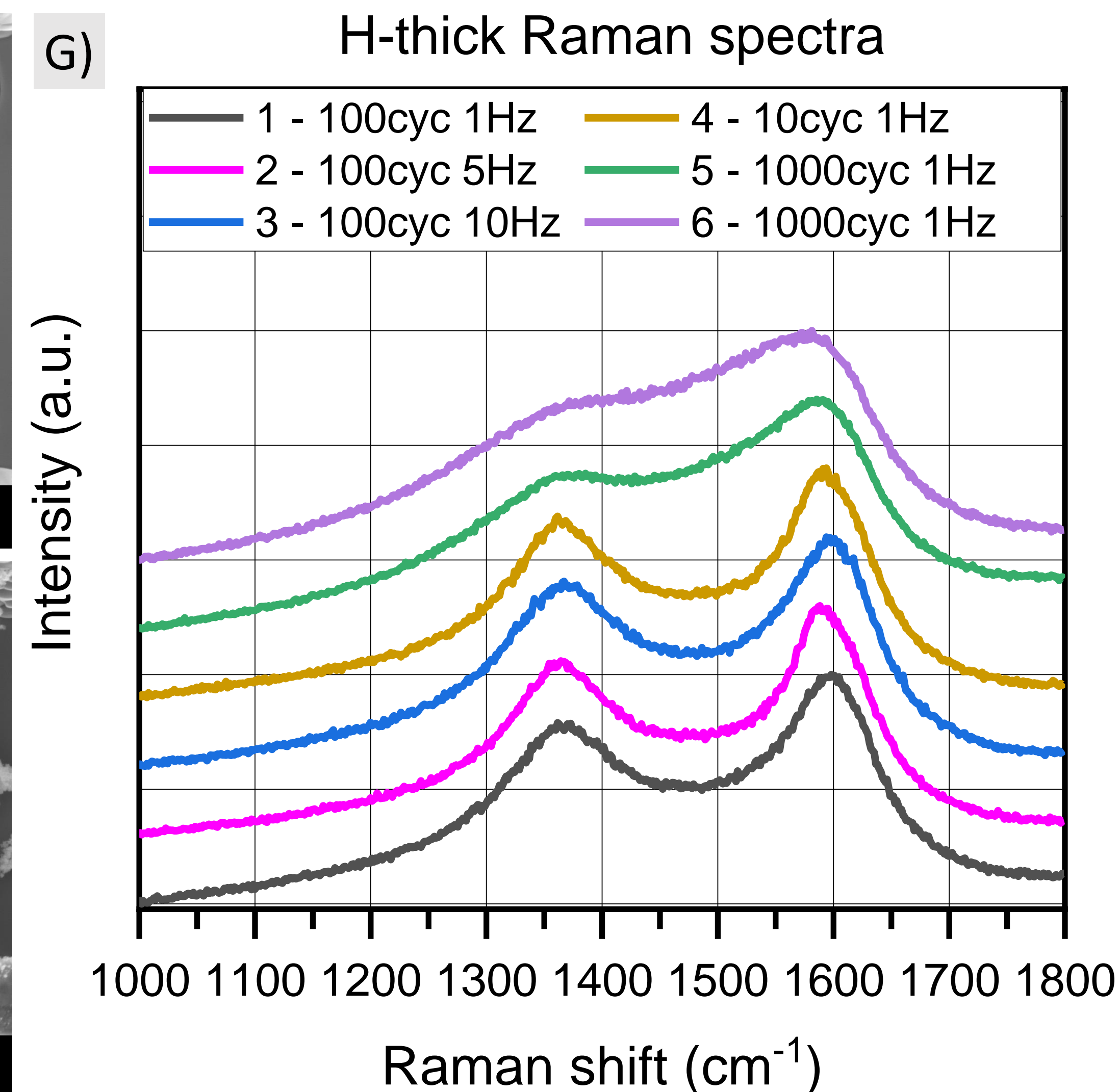
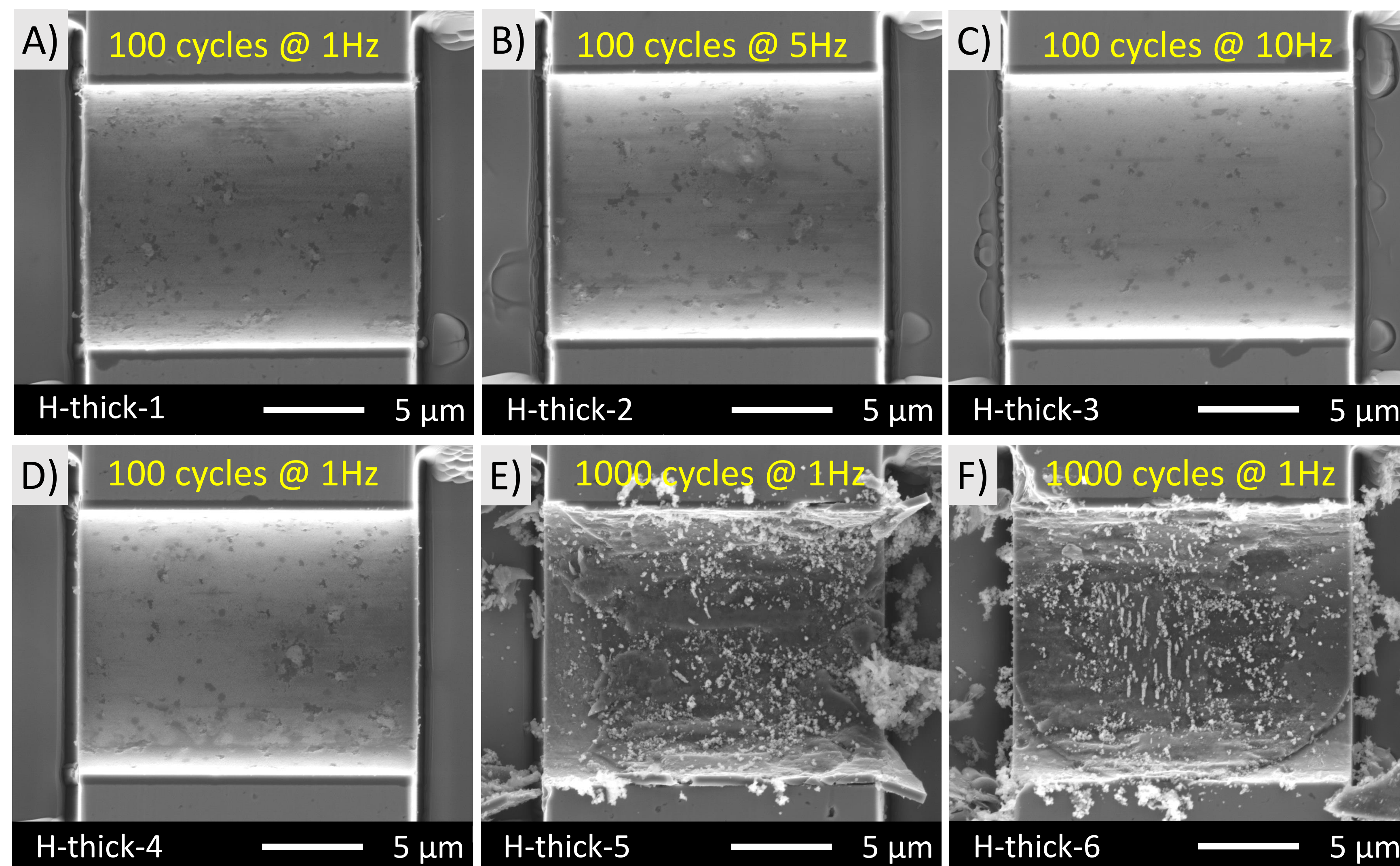


Figure 9 – A-F) SEM images of all H-thick tribo-surfaces. Smooth surfaces suggest adhesive friction mechanisms. Rough surfaces with third body debris suggests a transition to abrasive friction. F) H-thick-6 shows ejected PyC fragments at the corner edges and rolled third body particles at the center. G) Raman spectra of all six samples with clear peak broadening of the 1000 cycle samples

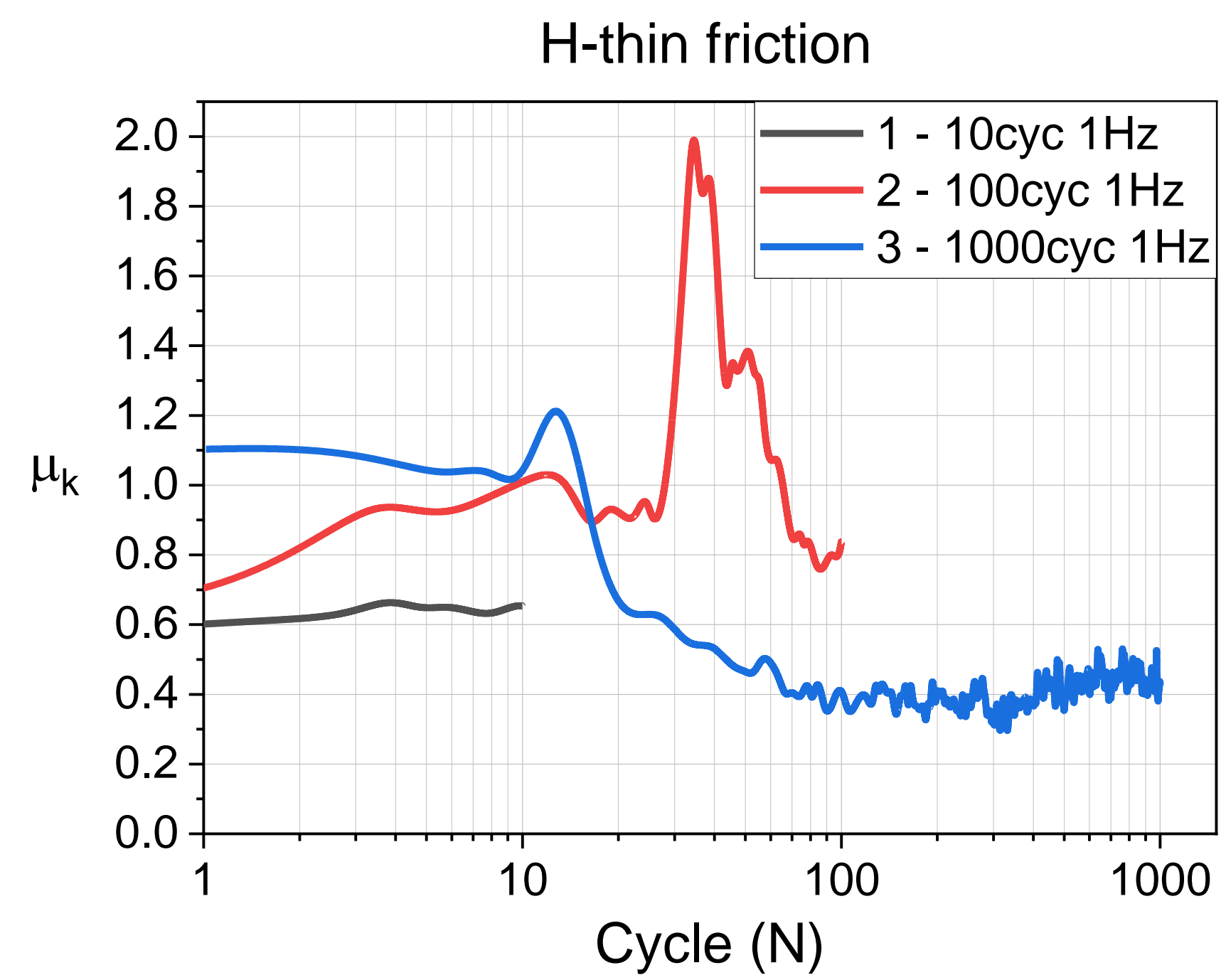


Figure 10 – Friction data for all H-thin composite micro-sliders at 1Hz. The first 100 cycles show relatively high values with some erratic behavior that decay to a steady-state regime.

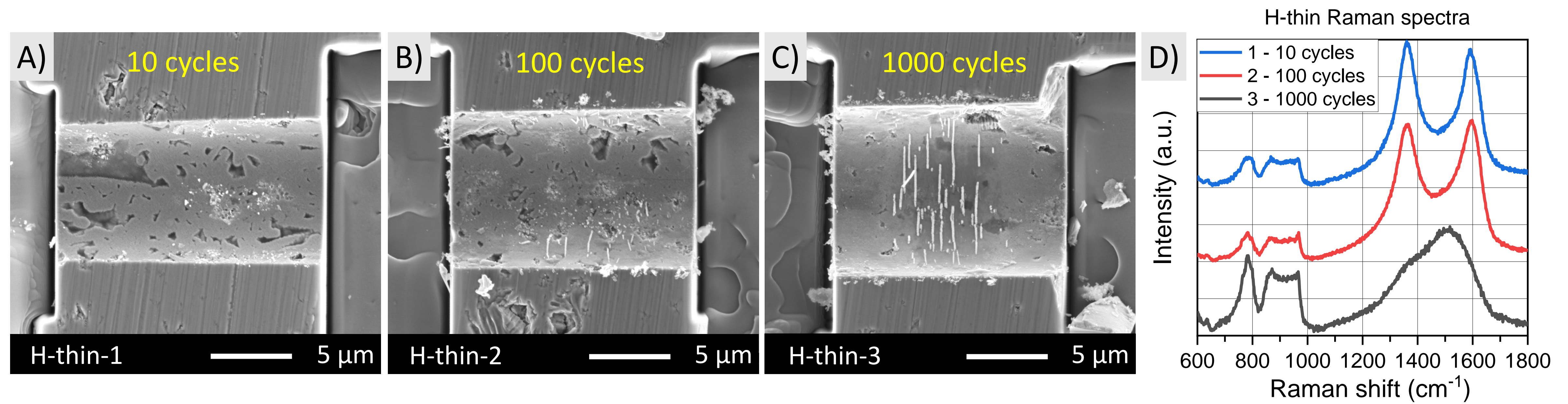


Figure 11 – SEM images of all H-thin tribo-surfaces. Progressive rolled third body particle evolution is observed from 10 to 1000 cycles D) Raman spectra showing increased intensity from underlying SiC and clear degradation of the carbon material after 1000 cycles.

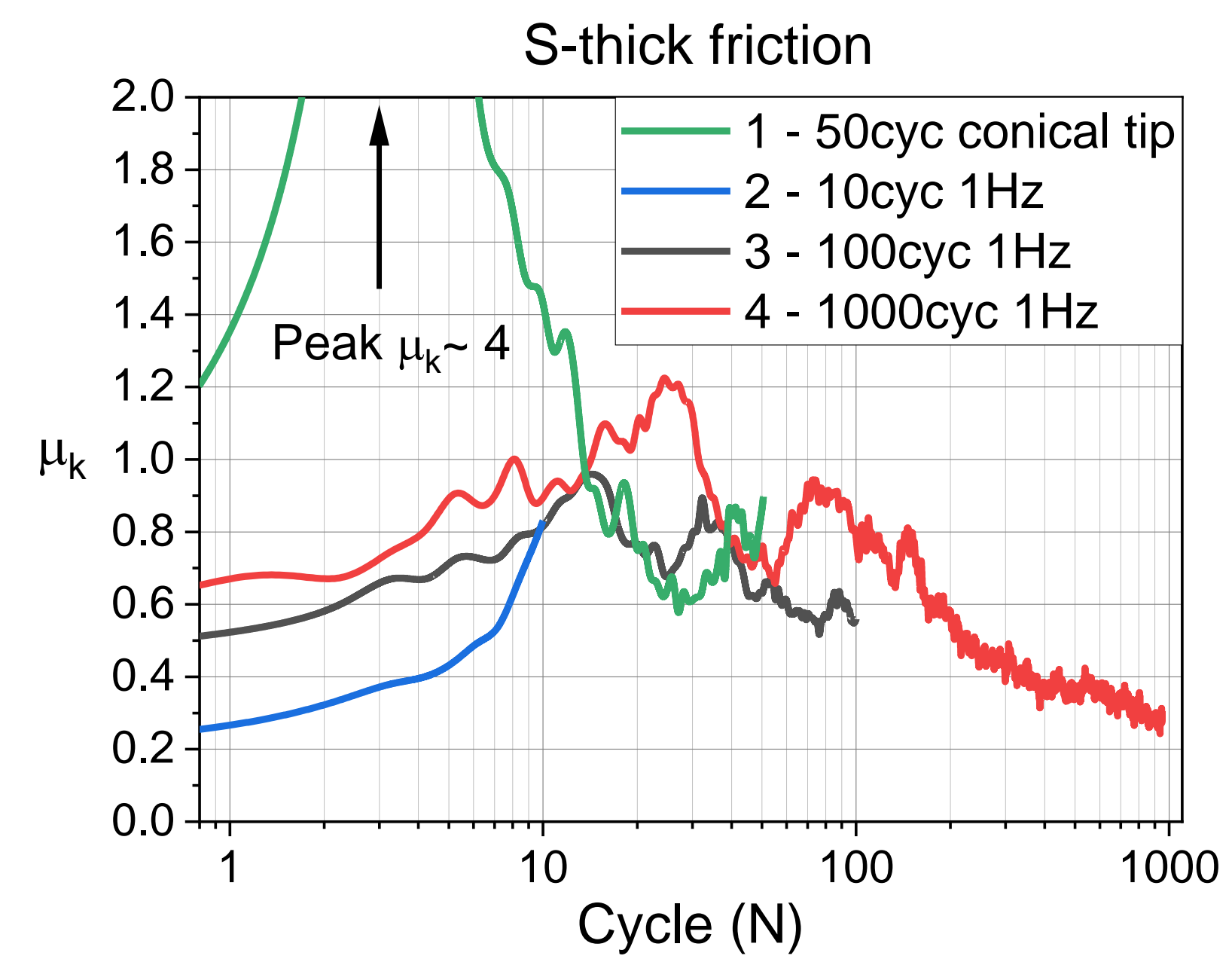


Figure 12 - Friction data for all S-thick composite micro-sliders.

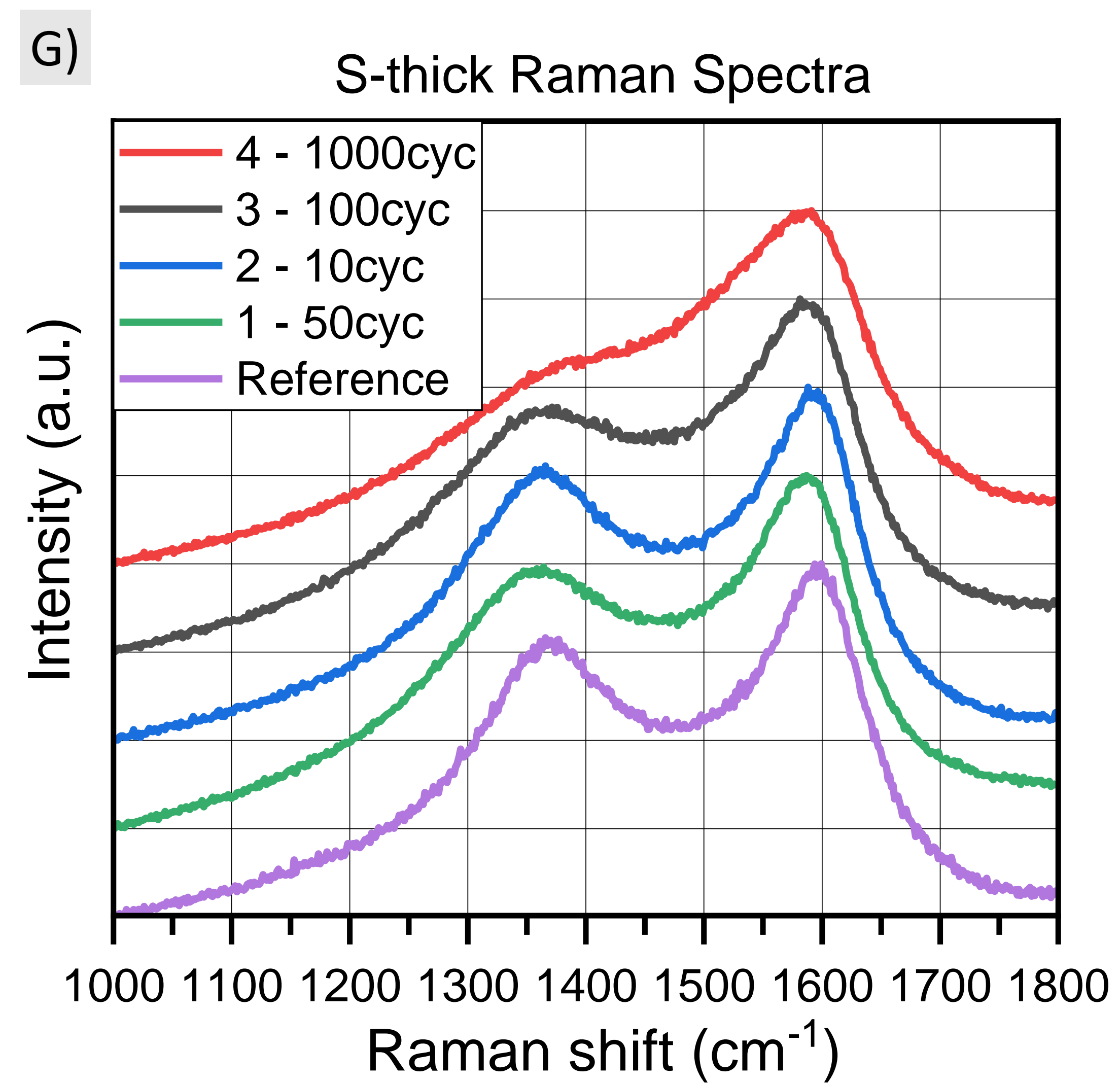
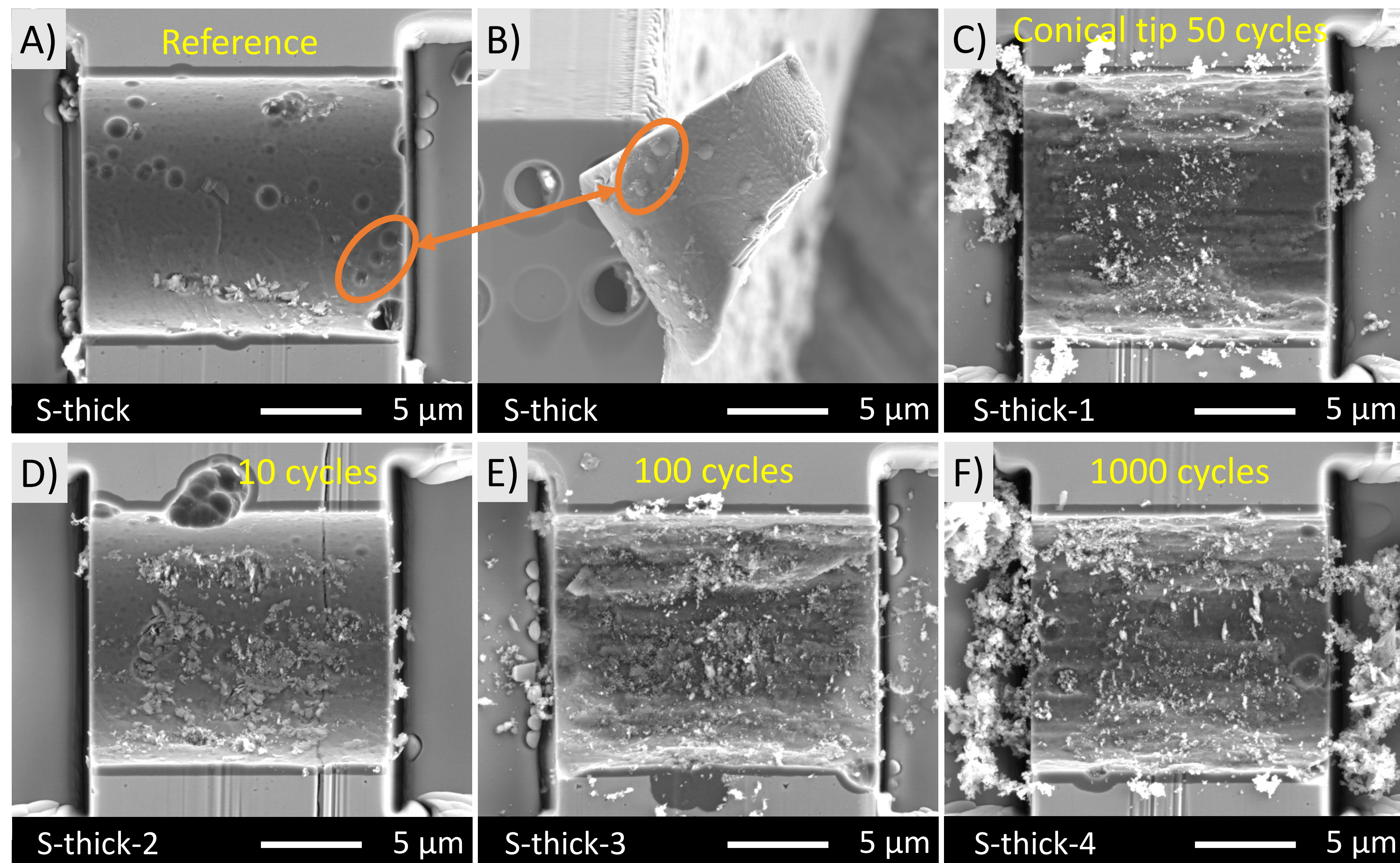


Figure 13 – A & B) Reference PyC fracture surface showing pre-existing CVI nodule defects. C-F) SEM images of S-thick tribo-surfaces. Wear debris is observed for all cases. G) Raman spectra show peak broadening with increased cycles.

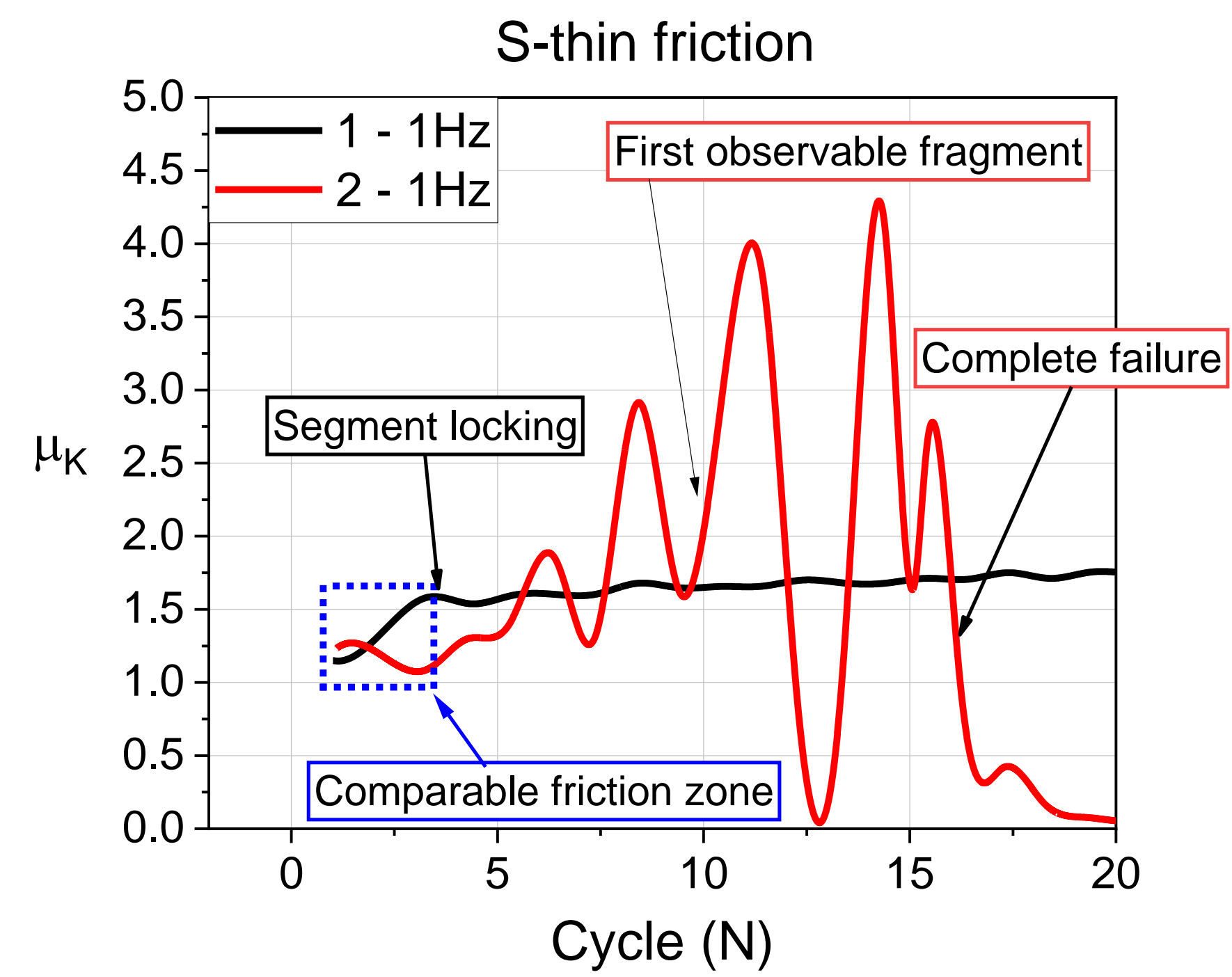


Figure 14 – Friction data for the first 20 cycles of S-thin composite micro-sliders. Locking and failure events are highlighted based on video evidence.

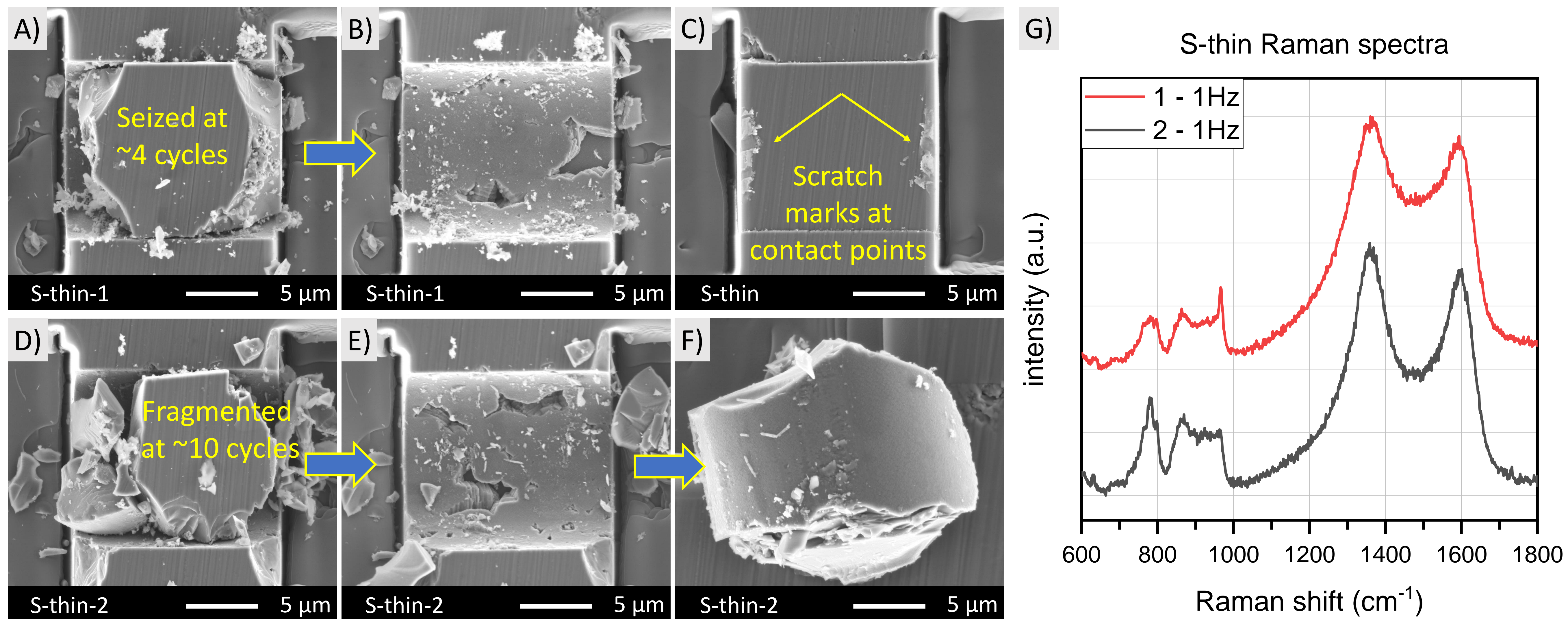


Figure 15 – A,B) S-thin-1 before and after the segment was removed to reveal the tribo-surface. Fragmentation of the fiber segment as well as underlying porosity are observed. C) Shows a S-thin segment that did not displace. Scratch marks are observed at the gripper/segment contact D,E) S-thin-2 before and after images showing the segment fragmentation and tribo-surface. F) Shows the underside of the S-thin-2 segment after it was removed with evidence of PyC rolling.

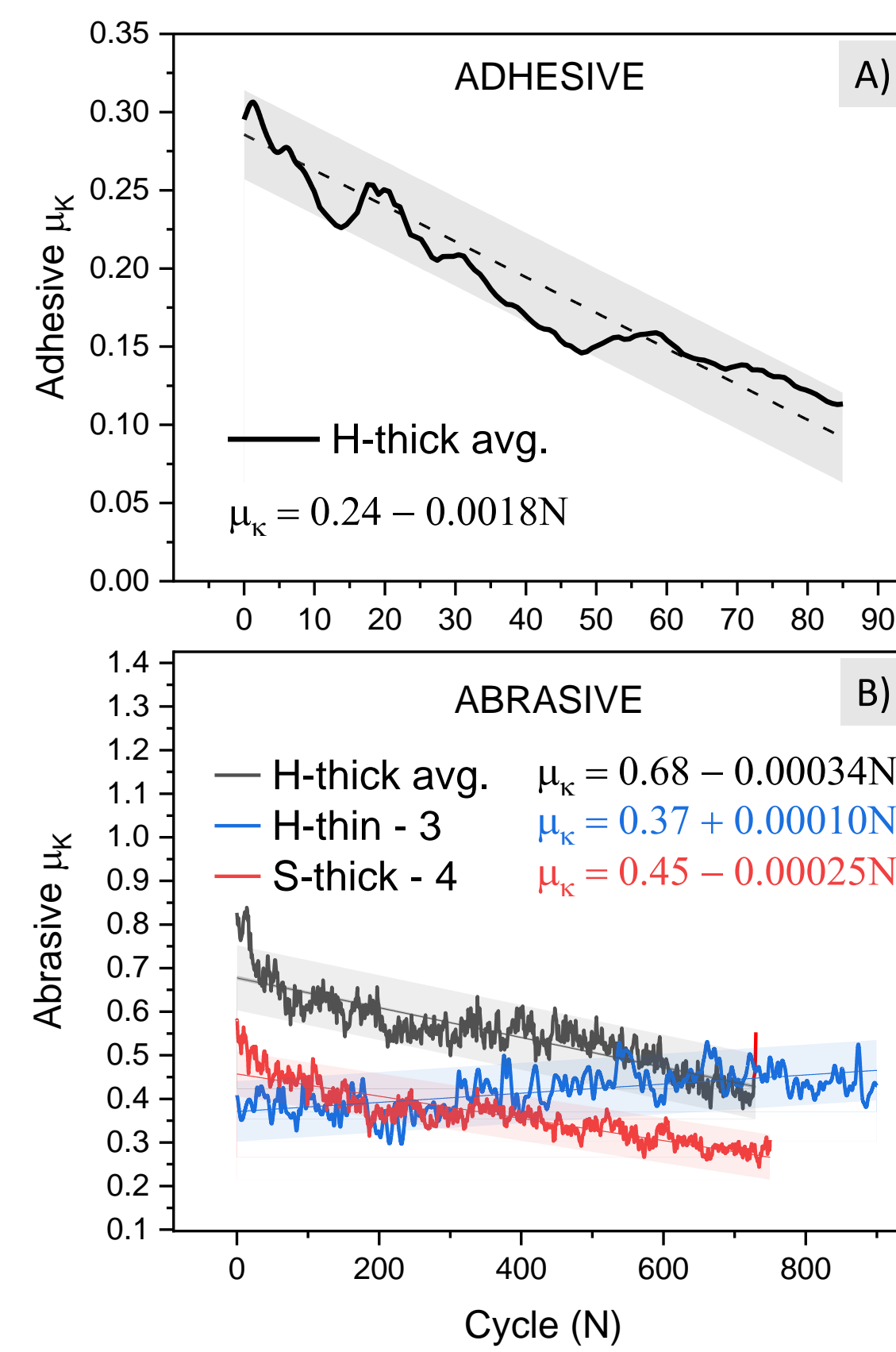


Figure 16 – A) Average steady-state kinetic friction coefficient for the adhesive regime observed in composite H-thick B) Steady-state friction coefficients for the adhesive regimes observed in H-thick, H-thin, and S-thick.

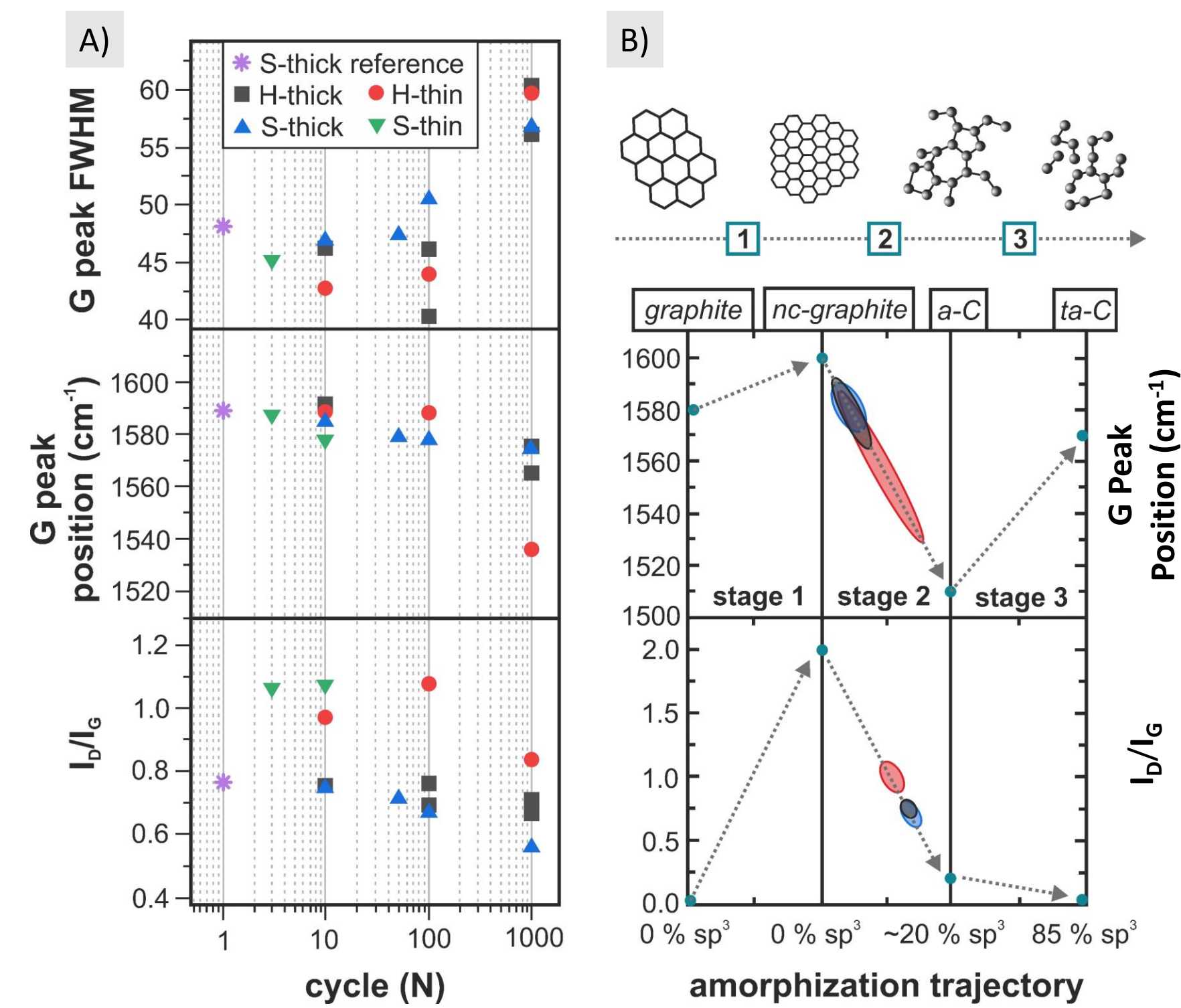


Figure 17 – A) Experimental Raman values as a function of cycle for all micro-sliders. B) Ferrari et al. Amorphization trajectory through graphite, nanocrystalline (nc) graphite, amorphous carbon (a-C), and to amorphous tetrahedral carbon (ta-C), reproduced and adapted with permission from ref [39], copyright American Physical Society 2000.